

Non-ideal magnetohydrodynamics on a moving mesh

Federico Marinacci^{1*}, Mark Vogelsberger^{1†}, Rahul Kannan^{1,2‡}, Philip Mocz^{3‡},
Rüdiger Pakmor⁴, and Volker Springel^{4,5,6}

¹*Kavli Institute for Astrophysics and Space Research, Massachusetts Institute of Technology, 77 Massachusetts Ave, Cambridge, MA 02139, USA*

²*Harvard-Smithsonian Center for Astrophysics, 60 Garden Street, Cambridge, MA 02138, USA*

³*Department of Astrophysical Sciences, Princeton University, 4 Ivy Lane, Princeton, NJ, 08544, USA*

⁴*Heidelberger Institut für Theoretische Studien, Schloss-Wolfsbrunnengasse 35, 69118 Heidelberg, Germany*

⁵*Zentrum für Astronomie der Universität Heidelberg, Astronomisches Recheninstitut, Mönchhofstr. 12-14, 69120 Heidelberg, Germany*

⁶*Max-Planck-Institut für Astrophysik, Karl-Schwarzschild-Str. 1, D-85748, Garching, Germany*

Accepted 2018 February 12. Received 2018 February 10; in original form 2017 October 27

ABSTRACT

In certain astrophysical systems the commonly employed ideal magnetohydrodynamics (MHD) approximation breaks down. Here, we introduce novel explicit and implicit numerical schemes of ohmic resistivity terms in the moving-mesh code AREPO. We include these non-ideal terms for two MHD techniques: the Powell 8-wave formalism and a constrained transport scheme, which evolves the cell-centred magnetic vector potential. We test our implementation against problems of increasing complexity, such as one- and two-dimensional diffusion problems, and the evolution of progressive and stationary Alfvén waves. On these test problems, our implementation recovers the analytic solutions to second-order accuracy. As first applications, we investigate the tearing instability in magnetized plasmas and the gravitational collapse of a rotating magnetized gas cloud. In both systems, resistivity plays a key role. In the former case, it allows for the development of the tearing instability through reconnection of the magnetic field lines. In the latter, the adopted (constant) value of ohmic resistivity has an impact on both the gas distribution around the emerging protostar and the mass loading of magnetically driven outflows. Our new non-ideal MHD implementation opens up the possibility to study magneto-hydrodynamical systems on a moving mesh beyond the ideal MHD approximation.

Key words: magnetic fields – magnetic reconnection – (magnetohydrodynamics) MHD – methods: numerical – stars: formation

1 INTRODUCTION

Magnetic fields are an essential component of the Universe. They are present at all spatial scales (Vallée 1998; Ferretti et al. 2012; Beck & Wiełebinski 2013), and directly influence a large amount of processes that play a key role in shaping the properties of the objects populating the cosmos. Therefore, a complete understanding of many astrophysical phenomena requires taking into account the effects of magnetic fields on the dynamics of conducting gases (Ferrière 2001; Cox 2005) and charged relativistic particles (Fermi 1949; Kotera & Olinto 2011).

Numerical simulations represent the most comprehensive approach to describe the evolution of complex physical systems. The inclusion of magnetic fields in numerical astrophysical magnetohydrodynamical simulations often makes use of the so-called ideal magnetohydrodynamics (MHD) approximation (e.g. Fromang et al.

2006; Mignone et al. 2007; Stone et al. 2008; Dolag & Stasyszyn 2009; Pakmor et al. 2011; Pakmor & Springel 2013; Hopkins & Raives 2016). Under many circumstances, this approximation is an excellent description for the behaviour of partially ionized gases in the presence of magnetic fields. Indeed, simulations using this approach have become quite sophisticated, and are modelling systems of increasing complexity. These range from small-scale calculations studying the development of turbulence and the structure of the interstellar medium of galaxies (e.g. de Avillez & Breitschwerdt 2005; Iffrig & Hennebelle 2017) to larger scale simulations studying the origin and the evolution of magnetic fields in galaxies (e.g. Pakmor et al. 2014, 2017) and galaxy clusters (e.g. Dolag et al. 1999, 2002), and to large-scale cosmological simulations (Marinacci et al. 2015; Dolag et al. 2016; Marinacci & Vogelsberger 2016; Marinacci et al. 2017).

However, there are situations, especially at small spatial scales, e.g. below those of giant molecular clouds, where the ideal MHD approximation is not an accurate description of the underlying physics any more. Here the assumptions of ideal MHD break

* E-mail: fmarinac@mit.edu

† Alfred P. Sloan Fellow

‡ Einstein Fellow

down, and non-ideal MHD terms, such as ambipolar diffusion and ohmic resistivity, must be taken into account for a correct description of the physical system.

For example, in studies of galactic molecular clouds, it is well established that ambipolar diffusion, which arises in partially ionized plasmas, is a key physical process for the mechanism of star formation (e.g. Mestel & Spitzer 1956; Mouschovias 1976a,b; Shu et al. 1987) because it allows for the decoupling of neutral gas from magnetic fields (Basu & Ciolek 2004), which would otherwise hinder gravitational collapse and star formation. Ambipolar diffusion is also advocated to solve the so-called fragmentation crisis, i.e. the stabilizing effect that comparatively weak magnetic fields have on the fragmentation of a collapsing star-forming cloud (e.g. Hennebelle & Teyssier 2008). Moreover, ambipolar diffusion can have a non-negligible effect on MHD turbulence, by steepening the velocity and magnetic field power spectrum (Li et al. 2008) and changing the morphology of the velocity and density structures of the gas (Ntormousi et al. 2016). Finally, together with the Hall effect and ohmic resistivity, ambipolar diffusion is also relevant in proto-planetary discs, which are only partially ionized. In this case, the combination of these three non-ideal MHD effects can influence the development of the turbulence due to the magneto-rotational instability in such objects (Bai 2015), thus affecting the accretion rate on to the central star and the angular momentum transport within the disc (Lesur et al. 2014; Gressel et al. 2015; Béthune et al. 2017).

Ohmic resistivity is also important under various circumstances. In particular, it allows for magnetic reconnection, a change of topology of magnetic field lines that is prevented in ideal MHD due to flux conservation. At the reconnection points, ohmic resistivity generates intense Joule dissipation, which may power the heating of the solar corona (Parker 1983) or eruptive events in the Sun (see, e.g. Cheng et al. 2017). A crucial difficulty in the study of magnetic reconnection in simulations is due to the introduction of numerical resistivity, which is inherent to any discretization procedure. This non-physical resistivity may yield to reconnection phenomena that are entirely numerical in nature, substantially affecting the reliability of the simulations. This is particularly severe in the low-resistivity regime, which is usually the case in the modelling of real systems and that thus requires very high resolution to properly model the (small) spatial scales over which resistive effects are important.

The presence of ohmic resistivity may also render unstable otherwise stable configurations through the development of tearing instability modes (Furth et al. 1963). Another effect of a non-zero resistivity in the gas is the shortening of the decay time of long-term MHD turbulence in molecular clouds (Basu & Dapp 2010). Moreover, ohmic resistivity is a key physical process in the studies of the formation of discs around protostellar objects (Krasnopolsky et al. 2010). In this case, it can help in alleviating the so-called magnetic braking catastrophe, which is the suppression of the formation of rotationally supported discs in simulations modelling low-mass star formation in ideal MHD due to the high efficiency of angular momentum transport by the magnetic field. Indeed, this process seems to be effective on small scales (Dapp & Basu 2010), but to allow for the formation of larger circumstellar discs, other mechanisms, such as turbulent reconnection (Santos-Lima et al. 2012), have been proposed. Ohmic resistivity can also affect the efficiency and the mass loading of magnetically driven outflows in star-forming clouds (Machida et al. 2007; Matsushita et al. 2017), by weakening or even suppressing them compared to ideal MHD studies (Hennebelle et al. 2011; Seifried et al. 2012). Here ohmic resistivity weakens the coupling between the magnetic

fields and the gas in regions where the field dissipation, resulting from finite resistivity, is effective. The reduced coupling causes the inability of magnetic fields to drive outflows, which, on the other hand, are present even for weakly magnetized configurations in the ideal MHD case (see again Matsushita et al. 2017). However, the extent of these effects is uncertain and still debated. These uncertainties are associated to the difficulty in computing the exact value of the resistivity coefficient, which strongly depends on the detailed chemical composition and ionization state of the gas, in molecular clouds (see, e.g. Nakano et al. 2002).

Given the importance of non-ideal MHD processes, it is not surprising that many numerical implementations have been developed to include them in MHD simulations. The techniques adopted are very different, and single-fluid (e.g. Mac Low et al. 1995; Li et al. 2011; Masson et al. 2012), or multi-fluid (e.g. Falle 2003; Tilley & Balsara 2011) approaches, with a variety of time integration techniques, have been used. In this paper, we resort to a single-fluid approach and focus on the implementation of the ohmic resistive terms in the moving-mesh code AREPO (Springel 2010). We describe such an implementation for the Powell divergence cleaning and constrained transport (CT) MHD schemes. For both schemes we present an explicit and implicit time integration method for the treatment of the ohmic terms.

The paper is organized as follows. In Section 2, we describe the schemes that we have adopted to include the ohmic resistivity terms in AREPO, differentiating between the explicit (Section 2.1) and implicit time integration (Section 2.2) cases. In Section 3 we test our implementation on a variety of test problems. In Sections 4 and 5 we present first non-ideal MHD applications by studying magnetic reconnection and the gravitational collapse of a rotating magnetized cloud, respectively. Finally, in Section 6 we summarize our results.

2 METHODS

We implement the ohmic diffusion term in AREPO for two different numerical MHD techniques. The first one (Pakmor et al. 2011; Pakmor & Springel 2013) evolves the MHD equations using the Powell et al. (1999) 8-wave approach to control divergence errors. The second method (Mocz et al. 2014, 2016) implements the CT technique in AREPO, which has the advantage of enforcing the $\nabla \cdot \mathbf{B} = 0$ constraint to machine precision. The CT scheme in AREPO evolves the cell-centred magnetic vector potential rather than a face-centred magnetic field. For the implementation of the ohmic diffusion term we restrict ourselves to a constant gas resistivity although this can easily be extended to the case of a spatially varying resistivity. Finally, for each MHD scheme, we present an explicit and implicit time integration method of the ohmic diffusion terms, discussing only the MHD equations directly affected by the introduction of such terms, as described in the following subsections. The interested reader can find a complete description of the MHD treatment in AREPO in method papers cited above.

2.1 Explicit time integration

In the limit of spatially constant gas resistivity η the induction equation is given by¹

$$\frac{\partial \mathbf{B}}{\partial t} - \nabla \times (\mathbf{v} \times \mathbf{B}) - \eta \nabla^2 \mathbf{B} = 0, \quad (1)$$

or in terms of the vector potential $\mathbf{B} = \nabla \times \mathbf{A}$, under the Coulomb gauge $\nabla \cdot \mathbf{A} \equiv 0$:

$$\frac{\partial \mathbf{A}}{\partial t} - (\mathbf{v} \times \mathbf{B}) - \eta \nabla^2 \mathbf{A} = 0. \quad (2)$$

A non-zero resistivity η further modifies the energy conservation equation to

$$\frac{\partial(\rho e)}{\partial t} + \nabla \cdot \{(\rho e + p)\mathbf{v} - (\mathbf{v} \cdot \mathbf{B})\mathbf{B} + \eta(\mathbf{J} \times \mathbf{B})\} = 0. \quad (3)$$

In the previous equations ρ is the gas density, e the gas total energy per unit mass, P the gas pressure, \mathbf{v} the gas velocity, \mathbf{B} the magnetic field, $\mathbf{J} = \nabla \times \mathbf{B}$, and the term $\eta(\mathbf{J} \times \mathbf{B})$ represents the heat added to the system due to the dissipation of the magnetic field through ohmic resistivity.

Equations (1)-(3) can be integrated in time in an explicit way by adding the contribution of the ohmic diffusion terms to the ideal MHD fluxes. We first focus on the induction equations. The diffusive terms have the form $\nabla \cdot \mathbf{F}_d$, where

$$\mathbf{F}_d = \begin{cases} -\eta \nabla \mathbf{B} \\ -\eta \nabla \mathbf{A}. \end{cases} \quad (4)$$

For a finite volume discretization the flux across a face shared by the mesh generating points i and j becomes after the application of Gauss' theorem

$$\mathbf{F}_d = \begin{cases} -\eta \frac{\mathbf{B}_i - \mathbf{B}_j}{r_{ij}} a_{ij} \\ -\eta \frac{\mathbf{A}_i - \mathbf{A}_j}{r_{ij}} a_{ij}, \end{cases} \quad (5)$$

where \mathbf{B}_i , \mathbf{A}_i are the time-extrapolated values of the magnetic field or the magnetic vector potential of cell i , r_{ij} is the distance between the mesh-generating points and a_{ij} is the area of the face. The expressions of equation (5) are then added to their ideal MHD counterpart before the flux limiting procedure and the time evolution of the system is applied.

For the ohmic heating term in the energy equation (3) the procedure is similar. To achieve second order accuracy in the computation of the heat flux across a given face shared between the mesh generating points i and j , we first compute the term $\eta(\mathbf{J} \times \mathbf{B})$ for the two cells and we subsequently take their average as the resulting second-order flux. The expression for the heat flux is thus given by

$$\eta \frac{(\mathbf{J}_i \times \mathbf{B}_i) + (\mathbf{J}_j \times \mathbf{B}_j)}{2} \cdot \frac{\mathbf{r}_{ij}}{r_{ij}} a_{ij}, \quad (6)$$

with the symbols having the same meaning as in equation (5). Please note that other second-order discretizations are possible for these terms. For instance, the cross product can be taken *after* the average values of \mathbf{J} and \mathbf{B} are evaluated. However, tests on the propagation of an Alfvén wave (see Sec. 3.2 for the set-up of the test) show that the results obtained with this latter scheme are equivalent to the ones given by equation (6).

¹ Throughout the paper, we express magnetic field intensities in the Lorentz-Heaviside system of units.

The relative simplicity of explicit schemes has made them a popular choice in most of the available implementations of non-ideal MHD terms (e.g. Masson et al. 2012). However, the major drawback of explicit schemes is the rather restrictive time-step criterion that must be imposed for the scheme to be numerically stable. We enforce this by limiting the time-step of any given gas cell to

$$\Delta t = \min \left(\Delta t_{\text{MHD}}, \frac{\xi \Delta r^2}{\eta} \right), \quad (7)$$

where Δt_{MHD} is the time-step computed for the ideal MHD part of the calculation and the second term is the diffusive time-step that is composed of a pre-factor $\xi = 0.2$, the fiducial cell radius Δr , computed as the radius of the sphere having the same volume as the Voronoi cell (or circle having the same area for two-dimensional (2D) configurations; in case of 1D Voronoi tessellations it is the cell size), and the ohmic diffusion coefficient η . The quadratic dependence on the cell size, contrary to the linear dependence in the case of the ideal MHD timestep criterion, renders the explicit non-ideal MHD scheme computationally expensive for high-resolution simulations.

2.2 Implicit time integration

The intrinsic timestep limitations of explicit time integration methods can be avoided by employing an implicit scheme that does not request such a stringent timestep criterion. We follow the implementation presented in Kannan et al. (2016, 2017), where an implicit scheme for anisotropic heat diffusion has been presented. The implementation of ohmic diffusion is simplified by the fact that the ohmic diffusion equations are isotropic such that many of the aspects described in Kannan et al. (2016), like the slope limiting procedure of the transverse diffusion fluxes, are not required in our case.

We start from the discretized form of equation (1) – the case of equation (2) follows naturally by replacing the magnetic field with the vector potential – in a finite volume sense by considering only the diffusive terms. After applying Gauss' theorem for cell i this can be cast into the form

$$\frac{\partial \mathbf{B}_i}{\partial t} = \frac{\eta}{V_i} \sum_{j \neq i} \frac{\mathbf{B}_j - \mathbf{B}_i}{r_{ij}} a_{ij}, \quad (8)$$

where the index j runs over all the neighbours of cell i and the meaning of the symbols is the same as in the previous equations (V_i is the volume of the i -th cell).

To advance equation (8) in time we use two methods. The first one is a first-order backwards Euler discretization, which we can write as

$$\frac{\mathbf{B}_i^{t+\Delta t} - \mathbf{B}_i^t}{\Delta t} = \frac{\eta}{V_i} \sum_{j \neq i} \frac{\mathbf{B}_j^{t+\Delta t} - \mathbf{B}_i^{t+\Delta t}}{r_{ij}} a_{ij}. \quad (9)$$

To solve equation (9) we recast it in the form

$$\mathbf{B}_i^{t+\Delta t} - \Delta t \sum_j M_{ij} (\mathbf{B}_j^{t+\Delta t} - \mathbf{B}_i^{t+\Delta t}) = \mathbf{B}_i^t, \quad (10)$$

where M_{ij} is a matrix with elements

$$M_{ij} = \begin{cases} \frac{\eta a_{ij}}{V_i r_{ij}} & \text{if } i \neq j \\ 0 & \text{if } i = j \end{cases}. \quad (11)$$

Equation (10) is a linear vector equation for the three components

of the magnetic field. We only focus on a generic component, but the same procedure applies similarly to the other components as well. We rewrite equation (10) for a generic component of the field in the i -th cell B_i as

$$B_i^{t+\Delta t} - \Delta t \sum_j M_{ij} (B_j^{t+\Delta t} - B_i^{t+\Delta t}) = B_i^t, \quad (12)$$

which, following the same procedure discussed in Kannan et al. (2016), can also be written in the form

$$\sum_j \left[\delta_{ij} \left(1 + \Delta t \sum_k M_{ik} \right) - \Delta t M_{ij} \right] B_j^{t+\Delta t} = B_i^t, \quad (13)$$

which is in the generic matrix form

$$CB = B_0. \quad (14)$$

This linear system can efficiently be solved via standard linear parallel solvers. To this end, we employ the HYPRE² library with the the generalized minimal residual (GMRES) iterative method (Saad & Schultz 1986) and an algebraic multigrid pre-conditioner (Henson & Yang 2002). We use a tolerance limit of $\epsilon_{\text{tol}} = 10^{-10}$ for the GMRES solver. It can be easily shown that the matrix C is (strictly) diagonally dominant. In the peculiar case of a structured (and static) mesh, in which the volume of each resolution element remains the same, the matrix is also symmetric and positive definite. This is the usual configuration in most of the test problems (see Section 3). In these configurations the matrix C will be well-conditioned and indeed convergence is reached after a few (~ 4 maximum) iterations of the GMRES solver. The conditioning properties of the matrix (and in particular strict diagonal dominance) are independent of the size of the time step. A direct estimation of the condition number of the matrix is difficult, but it can be assumed that for more distorted mesh topologies the matrix will become progressively more ill-conditioned. However, we would like to note that Arepo employs mesh regularization techniques that prevent unwanted and excessive mesh twisting and tangling (see Springel 2010), which therefore should also limit the magnitude of the condition number of the matrix C .

For improved accuracy we have also implemented a second-order Crank–Nicholson scheme (Crank et al. 1947). This can efficiently be implemented by considering

$$B_i^{t+\Delta t} - \frac{\Delta t}{2} \sum_j M_{ij} (B_j^{t+\Delta t} - B_i^{t+\Delta t}) = \tilde{B}_i^t, \quad (15)$$

where the right-hand side of equation (15) reads

$$\tilde{B}_i^t = B_i^t + \frac{\Delta t}{2} \sum_j M_{ij} (B_j^t - B_i^t). \quad (16)$$

We then solve the resulting linear system with the same iterative method used for the first-order Euler scheme. We note that contrary to the simple backwards Euler, which is our default choice, the Crank–Nicholson scheme may induce slowly decaying oscillations to the solution if the timestep is too large. To avoid the appearance of this, we limit the timestep according to equation (7) with safety factor $\xi < 0.5$ as derived by a von Neumann stability analysis. We point out that this procedure is performed only for the Crank–Nicholson scheme. In our simulations, should this timestep limitation become too computationally expensive, we resort to the more robust, but less accurate, Euler implicit time integration in

which no timestep limitation is present. With this approach our implicit treatment, unlike the explicit scheme, does never suffer from a too severe timestep constraint that would otherwise prevent performing high-resolution simulations of non-ideal MHD effects.

Finally, in the implicit integration scheme, the ohmic heating term is directly added to the gas thermal energy before diffusing the magnetic field or vector potential according to the equation

$$\frac{\partial u}{\partial t} = \eta \frac{\|\mathbf{J}\|^2}{\rho}, \quad (17)$$

where $\mathbf{J} = \nabla \times \mathbf{B}$, ρ is the gas density and u its thermal energy per unit mass. In particular, the new value for u_i for each cell is computed as

$$u_i^{t+\Delta t} = u_i^t + \Delta t \eta \frac{\|\mathbf{J}_i^t\|^2}{\rho_i^t}. \quad (18)$$

After the new magnetic field and internal energy values have been computed, the gas total energy and pressure are updated self-consistently. It is worth pointing out that the treatment for the ohmic heating term presented implies that the scheme is not strictly conservative and this can have an effect on the evolution of the simulated systems (see also Fig. 10). The implicit time integration schemes described above are used only on global time-steps (see Kannan et al. 2016, for details), which in combination with a less restrictive limitation on the time-step renders them significantly more efficient than their explicit counterpart, especially for non-ideal MHD applications in which resistivity effects become dominant.

3 TEST PROBLEMS

In this section, we test the implementation of the ohmic resistivity terms in AREPO on a series of problems of increasing complexity. For each problem, we present the initial conditions for the magnetic field and the vector potential, which is required for the initialization of the CT scheme. In all the test problems periodic boundary conditions will be imposed. In the case of the CT scheme, which evolves the vector potential, while the magnetic field is periodic the vector potential need not be. The mean magnetic field in the domain leads to a discontinuity in the vector potential across periodic boundaries. Therefore, the treatment of the vector potential in the CT scheme (Mocz et al. 2016) involves decomposing the vector potential into two parts by defining a periodic component of the vector potential and a component associated with the mean-field, which is discontinuous across boundaries. This is necessary as a discontinuity in the vector potential leads to an infinite value of the associated magnetic field with catastrophic effects on the runs. Finally, also in the case of ohmic diffusion the mean magnetic field in the simulated volume is a conserved quantity originating from a (non-periodic) vector potential static in time. Therefore, it is not necessary to evolve this part of the vector potential in time, and the associated mean magnetic field is simply added to the cell-centred field tracked by the simulation at the end of each CT mapping step (see Mocz et al. 2016, for details).

3.1 Gaussian pulse

We first test the implementation of resistive MHD terms in the simplified case where the dynamics of the gas is not followed. This is equivalent to assuming $\mathbf{v} \equiv \mathbf{0}$ at all times. The MHD equations

² <http://acts.nersc.gov/hypre>

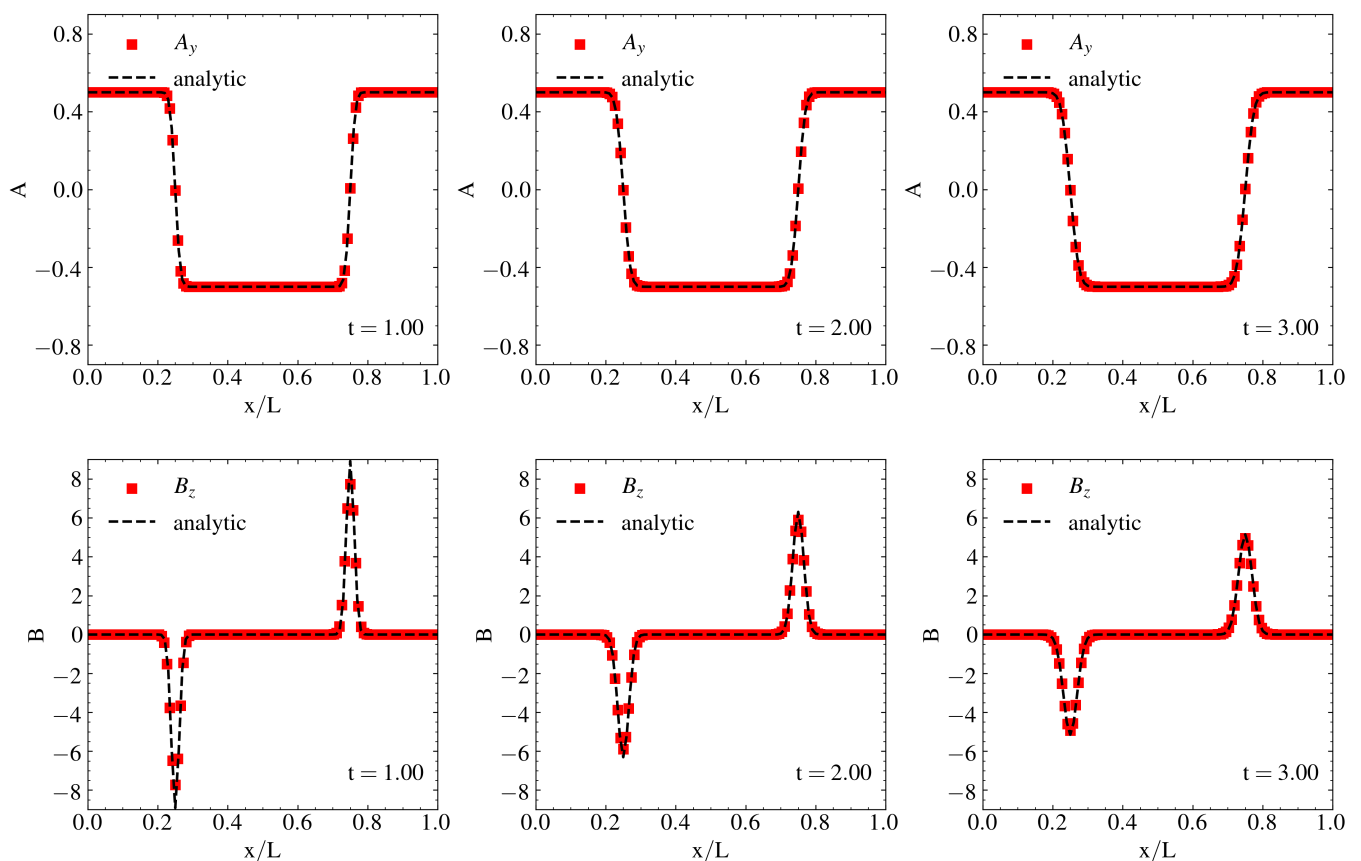


Figure 1. Time evolution of the diffusion of a 1D Gaussian magnetic field pulse with the implicit CT scheme. Both the evolution of the magnetic vector potential (top rows) and the associated magnetic field (bottom rows) are shown and compared to the analytic solution (dashed line). Time increases from the left-hand to right-hand side and is in units of the initial time ($t_0 = 10^{-3}$).

then reduce to

$$\frac{\partial \mathbf{B}}{\partial t} = \eta \nabla^2 \mathbf{B}. \quad (19)$$

Mathematically, equation (19) is an isotropic diffusion equation with diffusion coefficient η for each of the component of the magnetic field. A similar equation also holds for the vector potential \mathbf{A} in the CT scheme.

3.1.1 1D Gaussian pulse

To further reduce the complexity of the problem, we first simulate the diffusion of a 1D Gaussian pulse:

$$\mathbf{B}(\mathbf{x}) = \delta(x) \hat{e}_z, \quad (20)$$

where $\delta(x)$ is the Dirac delta function. The solution of this initial value problem at time t is the 1D heat kernel function

$$\mathbf{B}(\mathbf{x}, t) = \frac{1}{\sqrt{4\pi\eta t}} \exp\left(-\frac{x^2}{4\eta t}\right) \hat{e}_z. \quad (21)$$

To initialize this test, we sample equation (21) with 128 resolution elements at the initial time $t_0 = 10^{-3}$ and we assume $\eta = 1$. The test is carried out on the 1D domain $[0, L]$ with $L = 4$.

For the CT scheme we adopt the following vector potential for

this test

$$\mathbf{A}(\mathbf{x}) = \Theta(x) \hat{e}_y, \quad (22)$$

where $\Theta(x)$ is the Heaviside step function. The solution of this initial value problem at time t is the error function

$$\mathbf{A}(\mathbf{x}, t) = \frac{1}{2} \operatorname{erf}\left(\frac{x}{\sqrt{4\eta t}}\right) \hat{e}_y. \quad (23)$$

In order to use periodic boundary conditions, and since the ohmic diffusion operator is linear, we diffuse two of such steps by starting from the initial conditions

$$\mathbf{A}(\mathbf{x}) = \begin{cases} \Theta(x - 0.75) \hat{e}_y & \text{if } x > 0.5 \\ \Theta(0.25 - x) \hat{e}_y & \text{if } x \leq 0.5. \end{cases} \quad (24)$$

The time evolution of this vector potential gives rise to two Gaussian magnetic fields of opposite polarity centred at $x = 0.25$ and $x = 0.75$, respectively.

Fig. 1 presents the results of this test for the initial conditions described in equation (24) calculated with the implicit CT scheme³ with a 1D grid of 128 points. We chose this scheme since it for-

³ Unless otherwise stated the Crank–Nicholson scheme is used in this paper for the implicit time integration.

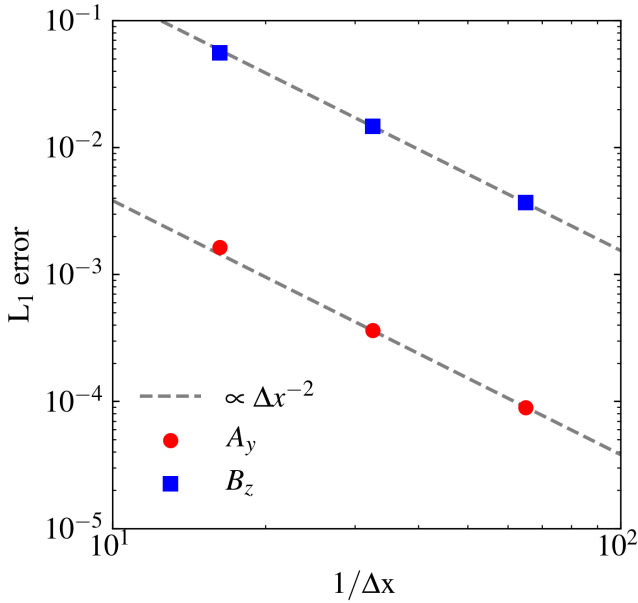


Figure 2. L_1 norm of the error as a function of resolution for the vector potential (red circles) and magnetic field (blue squares) of the 1D diffusion test, performed with the implicit CT scheme, at time $t = 4 \times t_0$. The grey dashed lines represent the expected scaling for a second-order scheme.

mally requires the diffusion of a discontinuous step function for $t = 0$, and therefore better illustrates the robustness of our implementation. All the other implementations of ohmic diffusion perform equally well in this test problem.

The panels show the evolution of the vector potential (top rows) and associated magnetic field (bottom rows) at different times in units of the initial time $t_0 = 10^{-3}$, indicated in the bottom right-hand corner of each panel. Red squares represent the numerical solution, whereas the black dashed lines represent the analytic solution. Our implementation correctly captures the evolution of the vector potential and the associated magnetic field even at the relatively low resolution used in this test problem. Only at the locations of the maximum and minimum magnetic field (at $x = 0.75$ and $x = 0.25$, respectively) the numerical values of the field are slightly underestimated with respect to the analytic solution, which however can be cured by adopting a higher resolution. This underestimation of the magnetic field intensities is less pronounced or absent altogether at later times.

In Fig. 2 we assess more quantitatively the performance of our scheme by showing the L_p error computed as (Pakmor et al. 2016)

$$L_p = \frac{1}{V} \left(\sum_{i=0}^{N_{\text{cells}}} |f_i|^p V_i \right)^{1/p}, \quad (25)$$

for the results presented in Fig. 1. In equation (25), V is the total simulated volume, V_i is the volume of the i -th cell, and f_i is the difference between the analytic and numerical solution in the cell i . In Fig. 2 we show the L_1 error ($p = 1$), for both the vector potential (red squares) and the magnetic field (blue circles), as a function of the mesh resolution expressed as the inverse of the mean cell size $1/\Delta x$. We note that we adopt these choices for stating the resolution in all similar figures quantifying the convergence of our

schemes that we will present below. The mean cell size Δx can be computed as the radius of a sphere (circle) having the same volume (area) of a given cell for 3D (2D) configurations depending on the problem analysed. We note that finer resolution corresponds to larger values of $1/\Delta x$. The grey dashed line represents the second-order scaling of the L_1 error expected for our schemes. We find that in this test problem the L_1 error follows exactly the scaling predicted for second-order convergence. Since the magnetic field is a derived quantity in the CT scheme (see Mocz et al. 2016), the amplitude of the L_1 error is larger than for the vector potential whose evolution is directly followed.

3.1.2 2D Gaussian pulse

The previous test problem assessed the accuracy of our ohmic diffusion scheme in a 1D set-up. We now increase the dimensionality by using as initial conditions a magnetic field of the form

$$\mathbf{B}(\mathbf{x}) = \delta(x)\delta(y)\hat{e}_z. \quad (26)$$

The solution of this initial value problem at time t is the 2D heat kernel

$$\mathbf{B}(\mathbf{x}, t) = \frac{1}{4\pi\eta t} \exp\left(-\frac{x^2 + y^2}{4\eta t}\right) \hat{e}_z. \quad (27)$$

To initialize the simulation, we sample equation (27) at the initial time $t_0 = 10^{-3}$, and we assume $\eta = 1$. The test is carried out on the 2D domain $[0, 1] \times [0, 1]$. The domain is partitioned in cells via a structured Voronoi mesh in which the mesh generating points are arranged in a 2D rhombic lattice. The lattice is built by using two interleaved Cartesian meshes of 32^2 points, separated by half the cell spacing, for a total of 2×32^2 resolution elements.

An explicit expression for the vector potential corresponding to the magnetic field presented in equation (27) can be found in polar coordinates

$$\mathbf{A}(\mathbf{x}, t) = -\frac{1}{2\pi R} \exp\left(-\frac{R^2}{4\eta t}\right) \hat{e}_\varphi, \quad (28)$$

or equivalently in Cartesian coordinates

$$\mathbf{A}(\mathbf{x}, t) = -\frac{y\hat{e}_x - x\hat{e}_y}{2\pi(x^2 + y^2)} \exp\left(-\frac{x^2 + y^2}{4\eta t}\right). \quad (29)$$

To initialize the test for the CT scheme, we use again the same mesh of 2×32^2 resolution elements on the 2D domain $[0, 1] \times [0, 1]$ adopted for the Powell scheme. Equation (29) is sampled on this mesh at the initial time $t_0 = 10^{-3}$, and we assume $\eta = 1$.

Fig. 3 illustrates the result of this test for the initial conditions described in equation (27) calculated with the implicit Powell scheme. We chose here the implicit Powell scheme, instead of the more complex implicit CT scheme, to demonstrate that our non-ideal MHD implementation is also working for the cleaning scheme. Again, we note that all the other schemes applied to this test problem essentially give the same results. The panels show the evolution of the magnetic field at different times (in units of the initial time $t_0 = 10^{-3}$) indicated in the top right-hand corner of each panel. The colour map shows the values of the field mapped linearly in the range $[0; 10]$, whereas the contour lines are placed at the values 1, 5, 5 and 10 (from the outside in). The upper right-hand quadrant of each panel shows the analytic solution obtained from equation (27), whereas in the rest of the plot the numerical solution is presented.

The implicit treatment of ohmic diffusion with the Powell scheme is able to correctly capture the evolution of the magnetic

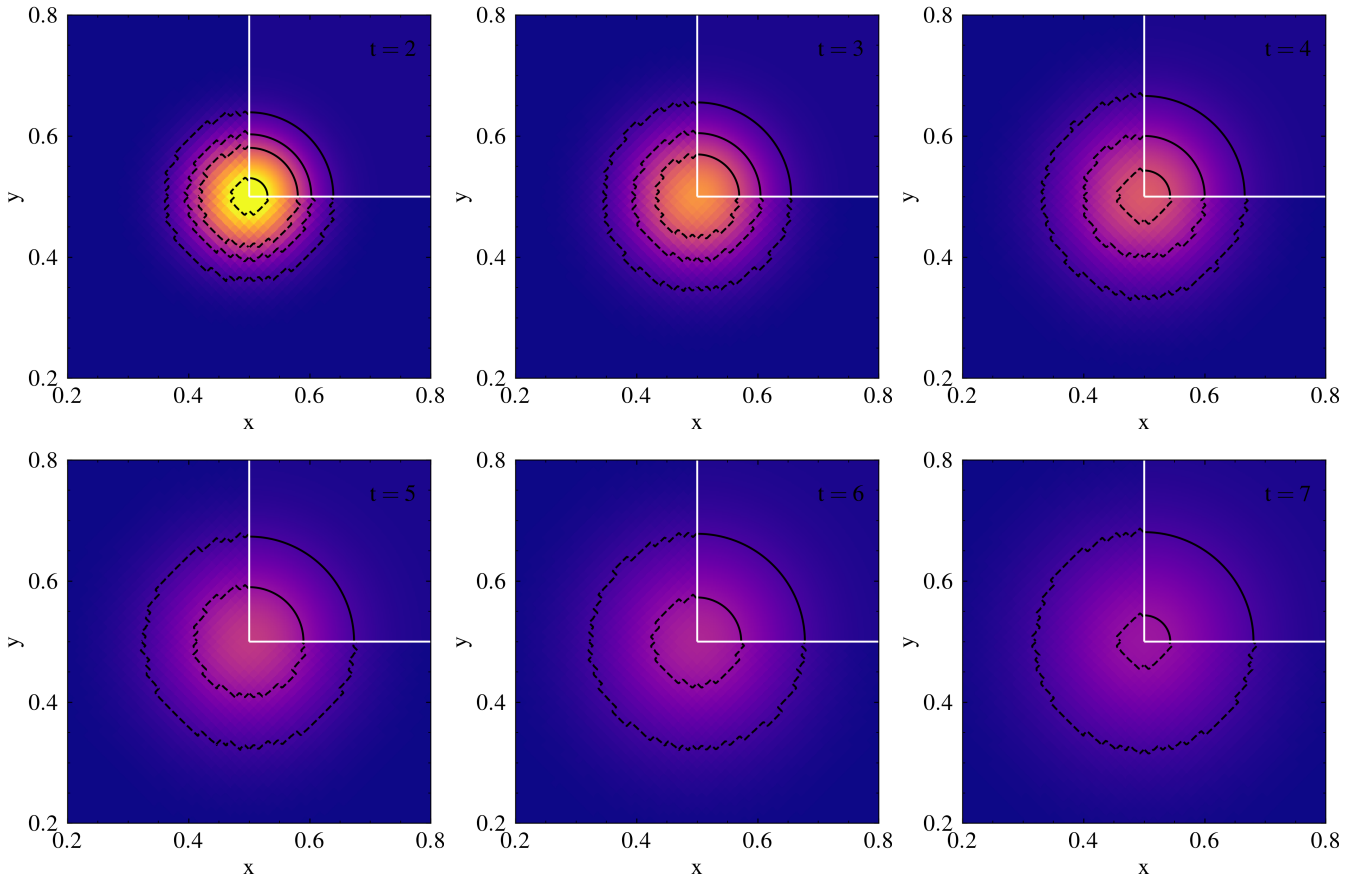


Figure 3. Time evolution of the diffusion of a 2D Gaussian magnetic field pulse evolved with the implicit Powell scheme. Contour levels are located at 10, 5, 3, and 1, from the innermost to the outermost. The upper right-hand quadrant of each panel shows the evolution of the analytic solution of this problem (see equation 27). Time, in units of the initial time $t_0 = 10^{-3}$, increases from the left to right-hand side and from the top to bottom as indicated in the legend.

field intensity with time. The diffusion of the field is visible in the panels as a decrease of the central magnetic field strength as a function of time. The contour levels clearly illustrate this trend. In particular, the highest contour shrinks in size with time, as the magnetic field diffuses out, and disappears in the second panel. Similarly, the second highest contour shrinks in size and disappears at time $t = 5 \times t_0$. We note that, contrary to the computation of the analytic solution, no smoothing of the simulation values has been applied to produce this figure; i.e. the magnetic field values of the cell closest to any given pixel has been assigned to that pixel. This has been done on purpose to show the structure of the underlying rhombic mesh. The structure is made more evident by the shape of the contour levels in the quadrants displaying the numerical solution, which unlike the smooth circular analytic contours, present a jagged shape along the cell boundaries. However, their spatial position is in excellent agreement with the analytic expectations.

Fig. 4 presents the L_1 error as a function of the mesh resolution for the implicit Powell scheme investigated in this test. The second-order convergence of the scheme, as indicated by the grey dashed line, is clearly visible. All the other schemes implemented in this work show the same behaviour when they are coupled with a second-order accurate time integrator.

3.2 Alfvén waves

We now test our implementation of the ohmic diffusion term in the presence of gas dynamics by studying the evolution of a circularly polarized Alfvén wave. The resistivity term in equations (1) and (2) causes the amplitude of the wave to decay exponentially, whereas the ohmic dissipation term added to the energy equation (3) leads to an increase of the thermal energy content of the gas via Joule heating. We test two cases: a progressive wave propagating along the negative z -direction (Section 3.2.1) and a stationary wave obtained as the superposition of two progressive waves propagating again along the z -axis but in opposite directions (Section 3.2.2). Both tests are presented for the implicit CT scheme since the additional step needed to reconstruct the magnetic field from the diffused vector potential makes it a more complex problem to test compared to the Powell method.

3.2.1 Progressive wave

We follow Masson et al. (2012) to initialize this test problem. In the case of a progressive wave, we evolve the following initial conditions in a 3D periodic domain of side length $L = 1$,

$$\mathbf{B}(\mathbf{x}) = \delta B [\cos(kz)\hat{e}_x - \sin(kz)\hat{e}_y] + B_0\hat{e}_z, \quad (30)$$

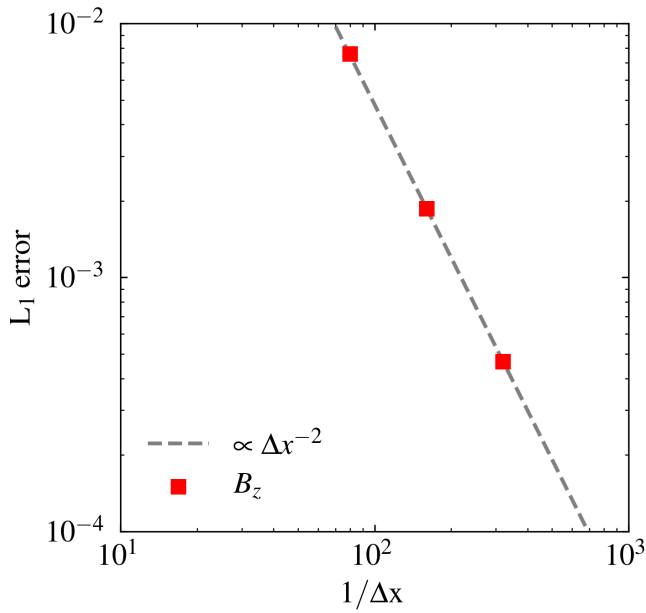


Figure 4. L_1 norm of the error as a function of resolution for the magnetic field in the 2D diffusion test at time $t = 4 \times t_0$ performed with the implicit Powell scheme. The grey dashed line represents the expected scaling for a second-order scheme.

$$\mathbf{v}(\mathbf{x}) = \delta v \{ [\omega_i \cos(kz) - \omega_r \sin(kz)] \hat{e}_x - [\omega_i \sin(kz) + \omega_r \cos(kz)] \hat{e}_y \}, \quad (31)$$

with

$$\begin{aligned} \delta v &= \frac{kB_0}{\rho_0 \omega^2} \delta B, & \omega^2 &= \omega_r^2 + \omega_i^2, & \omega_r &= -\frac{k^2 \eta}{2}, \\ \omega_i &= \sqrt{(kv_A)^2 - \omega_r^2}, & k &= 2\pi, & v_A &= \frac{B_0}{\sqrt{\rho_0}}. \end{aligned} \quad (32)$$

The wave will be evolving as

$$\mathbf{B}(\mathbf{x}, t) = e^{\omega_r t} \delta B [\cos(kz + \omega_i t) \hat{e}_x - \sin(kz + \omega_i t) \hat{e}_y] + B_0 \hat{e}_z, \quad (33)$$

$$\begin{aligned} \mathbf{v}(\mathbf{x}, t) &= e^{\omega_r t} \delta v \times \\ & \{ [\omega_i \cos(kz + \omega_i t) - \omega_r \sin(kz + \omega_i t)] \hat{e}_x \\ & - [\omega_i \sin(kz + \omega_i t) + \omega_r \cos(kz + \omega_i t)] \hat{e}_y \}, \end{aligned} \quad (34)$$

which is a planar, circularly polarized Alfvén wave in a clockwise direction from the source perspective.

The previous equations demonstrate how the amplitude of the wave is decaying exponentially at a rate equal to ω_r . The rate is faster for larger values of the resistivity η . Moreover, the frequency of the wave is decreased due to the resistivity in the system, which implies a lower propagation speed compared to the Alfvén speed. As a result of ohmic dissipation, the gas internal energy is expected to grow alongside an increase of the gas thermal pressure that can be described by (see again [Masson et al. 2012](#))

$$P(t) = 1 + (\gamma - 1) k^2 \delta B^2 \eta \frac{e^{2\omega_r t} - 1}{2\omega_r}, \quad (35)$$

with $\gamma = 5/3$ being the ratio of the specific heats of the gas. We

note that ω_r is a negative quantity. Therefore the increase in pressure reaches a maximum formally for $t \rightarrow +\infty$. This situation corresponds to the total dissipation of the initial magnetic and kinetic energy contained in the wave to thermal energy due to Joule heating. Moreover, the absence of any spatial dependence in the pressure expression implies that the heating is uniform throughout the simulated domain.

For the CT scheme, the periodic part of the vector potential originating the magnetic field of the progressive Alfvén wave (33)–(34) is given by

$$\mathbf{A}(\mathbf{x}) = \delta B \left[\frac{\cos(kz)}{k} \hat{e}_x - \frac{\sin(kz)}{k} \hat{e}_y \right] \quad (36)$$

and evolves as

$$\mathbf{A}(\mathbf{x}, t) = e^{\omega_r t} \delta B \times \left[\frac{\cos(kz + \omega_i t)}{k} \hat{e}_x - \frac{\sin(kz + \omega_i t)}{k} \hat{e}_y \right]. \quad (37)$$

The mean magnetic field is represented in this set-up by the z -component of equation (30). We initialize the simulation by assuming a uniform initial density $\rho_0 = 1$ and pressure $P_0 = 1$, a guide field in the z -direction $B_0 = 1$, $\delta B = 1$ and a resistivity $\eta = 2 \times 10^{-2}$. All other quantities can be derived from relations (32). For the mesh generating points of the Voronoi tessellation, we use a cubic body-centred lattice, composed by two interleaved Cartesian meshes of 32^3 points and separated by half the cell spacing, for a total of 2×32^3 resolution elements.

In Fig. 5, we present the results of this test problem for the implicit CT scheme on a static mesh. We show the amplitude of the two transverse components of the magnetic field (coloured squares) and of the guide field (black solid line) at different times, indicated in the top right-hand corner of each panel. The simulation results are compared to the analytic expectations, indicated by the dashed black lines in each panel. The simulation is run approximately for five periods of the wave. This is a time-scale over which the effect of ohmic dissipation is particularly noticeable.

The numerical results agree with the analytic expectations for this test. In particular, the guide field in the z -direction is not affected by the ohmic dissipation thus staying at its initial strength. The two transverse components, instead, clearly show an exponential decay in their amplitude, such that at the final time their maximum values are about a quarter of their initial amplitude. Also noticeable is the propagation of the wave towards decreasing values of the coordinate z . No phase offset is apparent in this test between the numerical values of the solution and the analytic estimates.

In the left-hand panel of Fig. 6 we quantify the exponential decay of the magnetic field by showing the time evolution of the volume-weighted rms values of the two transverse components of the magnetic field for the implicit CT scheme. This quantity gives an indication of the magnetic energy density contained within the simulated box in each of the magnetic field components, which is dissipated by ohmic resistivity. The y -component is offset by 0.1 from its true value to improve the clarity of the plot.

For the initial conditions used in this experiment we expect analytically that the mean rms values decrease exponentially in a characteristic time-scale ω_r , from an initial amplitude of $\sqrt{2}$. This trend is recovered in Fig. 6, where the simulation results (coloured squares) overlap well with the analytic expectations (black dashed line).

In the right-hand panel of Fig. 6 we show the L_1 error in the two transverse magnetic field components (coloured symbols) as

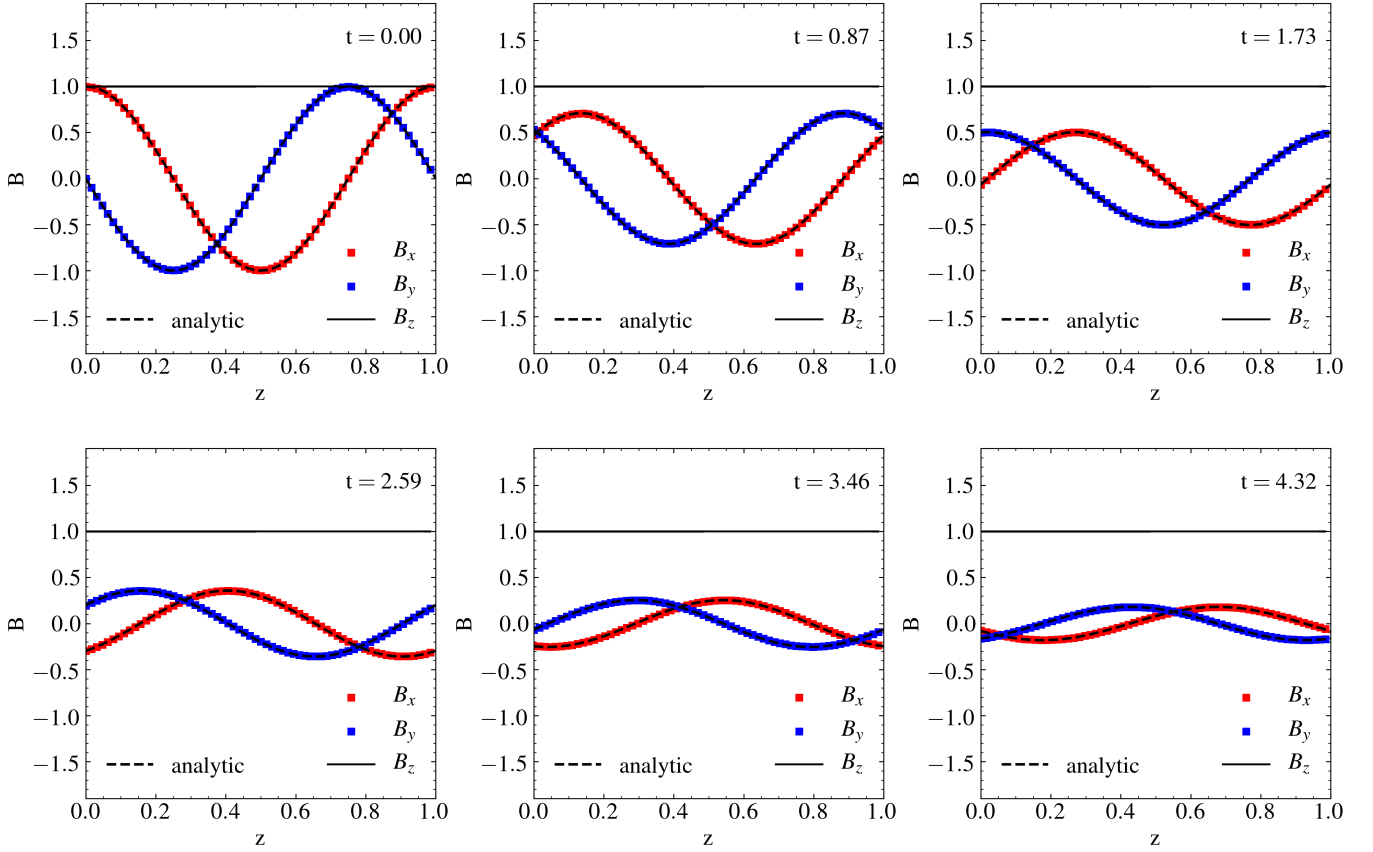


Figure 5. Time evolution of a progressive Alfvén wave in the presence of ohmic diffusion simulated with the implicit CT scheme. The panels show the evolution of the three components of the magnetic field (coloured symbols and black solid line) contrasted to the analytic solution (dashed line). The exponential decay in amplitude of the wave is clearly visible. The direction of wave propagation is the negative z -axis.

a function of the simulation resolution for the implicit CT scheme at $t = 0.74$. The grey dashed line shows the expected scaling for second-order convergence. The open coloured symbols indicate the results obtained for this test problem for the implicit Powell scheme run on a moving-mesh configuration in which the mesh generating points are free to move with the fluid motion. The figure clearly demonstrates the quadratic decrease of the L_1 error of the numerical solution with increasing resolution, thus signalling that even in this more complex case where gas dynamics must be taken fully into account, our implementations of the ohmic terms in AREPO perform as expected.

3.2.2 Stationary wave

The case of a stationary wave is obtained by linearly combining two progressive waves with equal weights (1/2) as described by equations (36), (30) and (31) propagating in opposite direction and thus with opposite ω_i . This results in

$$\mathbf{B}(\mathbf{x}) = \delta B [\cos(kz)\hat{e}_x - \sin(kz)\hat{e}_y] + B_0\hat{e}_z, \quad (38)$$

$$\mathbf{v}(\mathbf{x}) = -\delta v [\omega_r \sin(kz)\hat{e}_x + \omega_r \cos(kz)\hat{e}_y], \quad (39)$$

with all the symbols defined by equation (32). The wave will be evolving as

$$\mathbf{B}(\mathbf{x}, t) = e^{\omega_r t} \delta B [\cos(kz) \cos(\omega_i t) \hat{e}_x - \sin(kz) \cos(\omega_i t) \hat{e}_y] + B_0 \hat{e}_z, \quad (40)$$

$$\mathbf{v}(\mathbf{x}, t) = -e^{\omega_r t} \delta v \times \{ [\omega_i \sin(kz) \sin(\omega_i t) + \omega_r \sin(kz) \cos(\omega_i t)] \hat{e}_x + [\omega_i \cos(kz) \sin(\omega_i t) + \omega_r \cos(kz) \cos(\omega_i t)] \hat{e}_y \}. \quad (41)$$

We note that contrary to the previous case, the spatial and temporal dependences are separated such that the wave does not propagate. In particular, the location of the knots of the wave – where the magnetic field and velocity amplitude are zero – does not change with time. Only the amplitude of the wave is decaying exponentially at a rate equal to ω_r , as in the progressive case. Again, due to the ohmic dissipation, the gas internal energy increases and the gas thermal pressure evolves as (see Masson et al. 2012)

$$P(t) = 1 + \frac{(\gamma - 1)}{4} k^2 \delta B^2 \eta \left\{ \frac{e^{2\omega_r t} - 1}{\omega_r} + e^{2\omega_r t} \left[\frac{\omega_r \cos(2\omega_i t) + \omega_i \sin(2\omega_i t)}{\omega^2} \right] - \frac{\omega_r}{\omega^2} \right\}. \quad (42)$$

As in the progressive wave, ω_r is a negative quantity, which implies that for $t \rightarrow +\infty$ the pressure reaches a maximum value once the

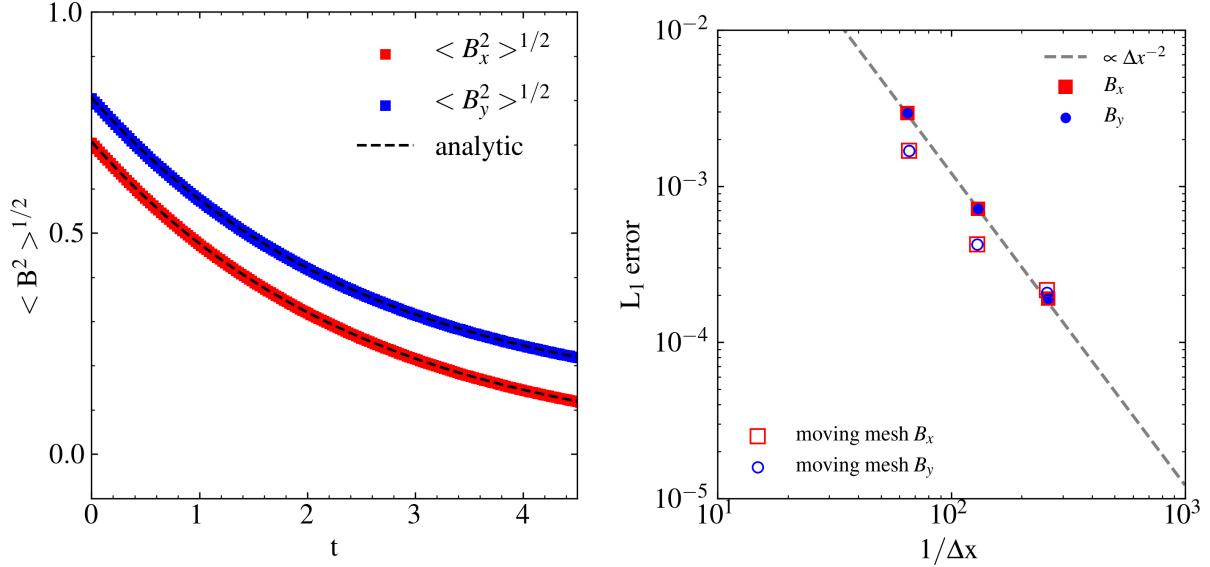


Figure 6. *Left-hand panel:* Time evolution of the average rms intensity of the transverse components of the magnetic field for the progressive Alfvén wave test simulation with the implicit CT scheme. The panel shows the evolution of these components (coloured squares) contrasted to the analytic solution (dashed line). The y -component of the magnetic field is offset from its true value to improve clarity. The exponential decay in the amplitude of the magnetic field is clearly visible. *Right-hand panel:* L_1 norm of the error as a function of resolution for the progressive Alfvén wave tests run with the implicit CT scheme at time $t = 0.74$. Different coloured symbols show the error of the individual components of the magnetic field as indicated in the legend, whereas the grey dashed line represents the expected scaling for a second-order scheme. Open symbols show the results obtained for the implicit Powell scheme run on a moving-mesh configuration. At high resolution the convergence becomes slower than second-order due to a significantly distorted mesh.

initial magnetic field is totally dissipated by resistive effects. The heating rate of the gas is independent of the position in this case as well.

For the CT scheme, the (periodic) vector potential originating a stationary Alfvén wave can be expressed as

$$\mathbf{A}(\mathbf{x}) = \delta B \left[\frac{\cos(kz)}{k} \hat{e}_x - \frac{\sin(kz)}{k} \hat{e}_y \right], \quad (43)$$

and its evolution is given by

$$\mathbf{A}(\mathbf{x}, t) = e^{\omega_r t} \delta B \times \left[\frac{\cos(kz) \cos(\omega_i t)}{k} \hat{e}_x - \frac{\sin(kz) \cos(\omega_i t)}{k} \hat{e}_y \right]. \quad (44)$$

The mean magnetic field is also represented in this set-up by the z -component of equation (38). The same set-up as in the progressive case is used in this test problem as well as for what concerns the values of both the initial gas properties and the grid geometry.

In Fig. 7, we present the results of this test for the implicit CT scheme on a static mesh. As in the previous case, we show the amplitude of the two transverse components of the magnetic field (coloured squares) and of the guide field (black solid line) at different times, shown in the top right-hand corner of each panel. The analytic solution is indicated by the dashed black lines in each panel. The simulation is run again approximately for five periods of oscillation of the wave to give ample time for ohmic diffusion to act.

This figure demonstrates that the numerical results agree very well with the analytic solution. As expected no change is visible in the guide field in the z -direction, which remains at the initial strength. On the other hand, the amplitude of the two transverse components decays exponentially as a function of time. At the final time displayed for this test problem they only reach one tenth

of their initial amplitude. This fact might appear surprising at first, given that the time-scale for dissipation ω_r is the same as in the progressive case ($e^{\omega_r t} \approx 0.18$ for $t = 4.32$). However, a closer inspection of equation (40) reveals that the magnetic field amplitude is further modulated by a $\cos(\omega_i t)$ term that accounts for this discrepancy.

The modulation due to this cosine term can be seen more easily if the mean energy content of the magnetic field is plotted as a function of time. We present this in the left-hand panel of Fig. 8, where the time evolution of the volume-weighted mean rms values of the two transverse components of the magnetic field is shown for the implicit CT scheme. The y -component of the field is offset by 0.2 from its true value to improve the clarity of the plot. We expect an exponential decay of the field amplitude on a characteristic time-scale ω_i starting from an initial amplitude of $\sqrt{2}$. It is evident from the figure that both the numerical (coloured squares) and analytical (black dashed line) solutions follow this expected trend and that they are in agreement with one another. In addition to the exponential decay, the modulation of the $\cos(\omega_i t)$ term is clearly visible as oscillations in the time evolution of the magnetic field rms values.

Finally, in the right-hand panel of Fig. 8 we present the L_1 error in the two transverse magnetic field components (coloured symbols) as a function of the simulation resolution for this set-up at $t = 0.74$. The grey dashed line indicates the scaling for second-order convergence, whereas the open coloured symbols show the results obtained for this test problem for the implicit Powell scheme run on a moving-mesh configuration. As in the progressive case, the convergence is second-order accurate. The plot also demonstrates that our implementation performs well when gas dynamics has to be followed to model self-consistently the evolution of the simulated system.

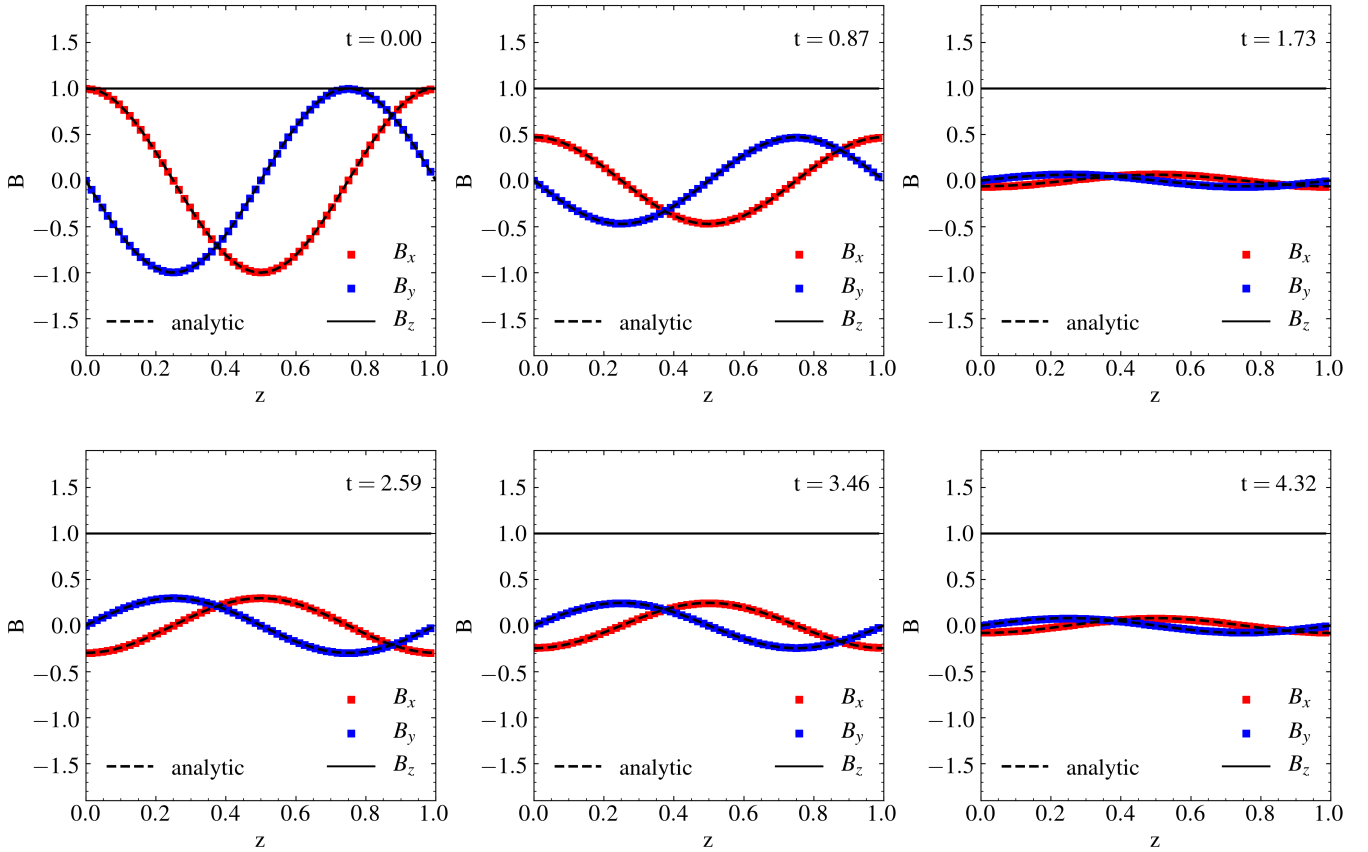


Figure 7. Time evolution of a stationary Alfvén wave in the presence of ohmic diffusion with the implicit CT scheme. The panels show the evolution of the three components of the magnetic field (coloured symbols and black solid line) contrasted to the analytic solution (dashed line). The exponential decay in amplitude of the wave is clearly visible.

4 MAGNETIC RECONNECTION

In this section, we present a first application of our ohmic resistivity implementation exploring the effects of magnetic reconnection. Magnetic reconnection is the rearrangement of the magnetic field topology that occurs in highly conducting plasmas with finite resistivity. During the reconnection phase, the energy that is present in the magnetic field can be rapidly converted into thermal and kinetic energy of the plasma. Therefore, this mechanism has been widely proposed as the key process that lies at the heart of eruptive events in the Sun (Zhu et al. 2016; Cheng et al. 2017; Seaton et al. 2017) or the heating of its corona (Parker 1983, see also Klimchuk 2006 and references therein).

To study this process, we simulate the so-called tearing instability (Furth et al. 1963). In this configuration, magnetic fields of opposite polarity are connected by a thin current sheet. Upon perturbing this configuration, reconnection of the field is triggered, which eventually leads to the formation of magnetic islands with increasing size that eventually coalesce (Landi & Bettarini 2012, and references therein for numerical work done on the instability).

To simulate the tearing instability we use an adapted version of the initial conditions presented in Landi et al. (2008). In particular, we use a 2D domain with side length $L_x = L_y = L = 6\pi$, which we simulate with 1024×3072 resolution elements. The larger number of resolution elements in the y -direction is necessary to resolve the steep gradients across the current sheets. The gas density is uni-

form and set to $\rho_0 = 1$. The initial conditions for this test start with a so-called Harris (1962) current sheet configuration, which is an equilibrium solution for ideal MHD equations (i.e. when the resistivity η is put to zero). To employ periodic boundary conditions throughout (see discussion at the beginning of Section 3), we use two of such current sheets of opposite polarity that are placed in the computational domain as

$$\mathbf{B}(y) = \begin{cases} B_0 \tanh \left[\delta \left(y - \frac{3L_y}{4} \right) \right] \hat{e}_x & \text{if } y > \frac{L_y}{2} \\ B_0 \tanh \left[\delta \left(\frac{L_y}{4} - y \right) \right] \hat{e}_x & \text{if } y \leq \frac{L_y}{2}, \end{cases} \quad (45)$$

where B_0 is the amplitude of the magnetic field at large distances from the current sheet and $\delta = 10$ is its characteristic thickness. Equilibrium is ensured by the condition

$$P + \frac{\|\mathbf{B}\|^2}{2} = \text{const}, \quad (46)$$

in which the gas thermal pressure P counterbalances its magnetic counterpart. This condition can be rewritten as

$$P(y) = \frac{\beta + 1 - \|\mathbf{B}\|^2}{2}, \quad (47)$$

and β can be interpreted as the ratio between thermal and magnetic

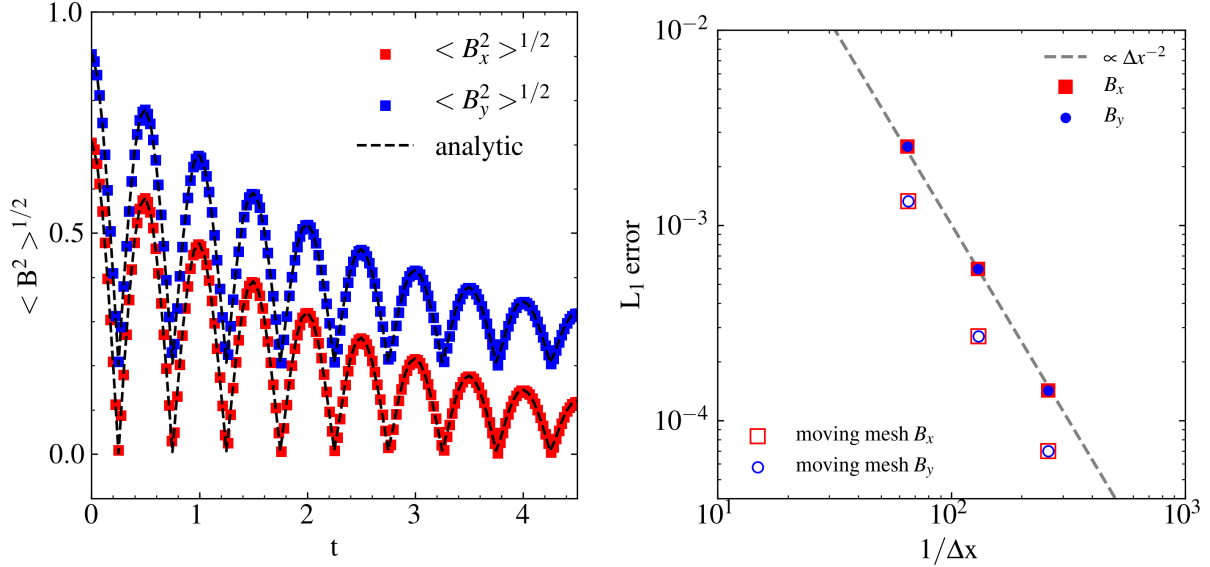


Figure 8. *Left-hand panel:* Time evolution of the average rms intensity of the transverse components of the magnetic field for the stationary Alfvén wave test simulation with the implicit CT scheme. The panel shows the evolution of this quantity contrasted to the analytic solution (dashed line). The y -component of the magnetic field is offset from its true value to improve clarity. The exponential decay in the amplitude of the magnetic field, modulated by a cosine function, is clearly visible. *Right-hand panel:* L_1 norm of the error as a function of resolution for the stationary Alfvén wave tests at time $t = 0.74$. Different coloured symbols show the error of the individual components of the magnetic field as indicated in the legend, whereas the grey dashed line represents the expected scaling for a second-order scheme. Open symbols show the results obtained for the implicit Powell scheme run on a moving-mesh configuration.

pressure in the plasma at large distances from the current sheet(s). We fix $\beta = 5$ in our runs, so magnetic fields are dynamically important in this set-up. We then perturb this equilibrium solution by adding a component in velocity as

$$\mathbf{v}(x, y) = \begin{cases} \epsilon \frac{\tanh \left[\delta \left(y - \frac{3L_y}{4} \right) \right]}{\cosh \left[\delta \left(y - \frac{3L_y}{4} \right) \right]} \sin(k_x x) \hat{e}_y & \text{if } y > \frac{L_y}{2} \\ \epsilon \frac{\tanh \left[\delta \left(\frac{L_y}{4} - y \right) \right]}{\cosh \left[\delta \left(\frac{L_y}{4} - y \right) \right]} \sin(k_x x) \hat{e}_y & \text{if } y \leq \frac{L_y}{2}, \end{cases} \quad (48)$$

where $\epsilon = 10^{-2}$, and $k_x = 2\pi m/L_x$. For the wavelength of the perturbation we chose $m = 7$, which Landi et al. (2008) showed to be the fastest growing mode. We employ Alfvénic units so that lengths are normalized to a characteristic scale L , which we assume to be unity, densities are normalized to a characteristic value $\rho_0 = 1$, magnetic fields are normalized to $B_0 = 1$, velocities are normalized to the Alfvén velocity $c_A = B_0/\sqrt{\rho_0}$, and times are normalized to $t_A = c_A/L$. The system is evolved up to the final time $t = 250 t_A$ with a resistivity $\eta = 2 \times 10^{-4}$.

For the CT scheme, a periodic vector potential that gives rise to the magnetic field in equation (45) is given by

$$\mathbf{A}(y) = \begin{cases} \frac{B_0}{\delta} \ln \cosh \left[\delta \left(y - \frac{3L_y}{4} \right) \right] \hat{e}_z & \text{if } y > \frac{L_y}{2} \\ \frac{B_0}{\delta} \left\{ C - \ln \cosh \left[\delta \left(\frac{L_y}{4} - y \right) \right] \right\} \hat{e}_z & \text{if } y \leq \frac{L_y}{2}, \end{cases}$$

where $C = 2 \ln \cosh(\delta L_y/4)$ is chosen to ensure the continuity of the vector potential at $y = L_y/2$. In the configuration that we have used in this test problem, the average magnetic field is zero. (49)

We present the results of this calculation in Fig. 9 for the implicit CT scheme on a static mesh. We point out that all our other schemes yield essentially the same results (see also Fig 10). In the top six panels we show the time evolution of the out-of-plane current density vector $J_z = \nabla \times \mathbf{B}$ at the time indicated in the top right-hand corner. The bottom six panels are the analogous figure for the evolution of the gas thermal pressure. At early times, it is evident how the gradient in the gas thermal pressure, which reaches its maximum values at the locations of the current sheets, balances the opposite gradient in the magnetic pressure – magnetic fields are zero at the sheet location, reaching their maximum amplitude far away from it (i.e. for $|y| \gg 1/\delta$). The thickness of the current sheets, indicated by the size of the coloured regions where J_z is not zero, slowly increases with time due to the presence of ohmic diffusion. At around $t = 100 t_A$ the linear perturbation added to the velocity also starts to be noticeable in J_z with its characteristic $m = 7$ pattern. At $t = 150 t_A$ the instability has fully developed in the non-linear regime and X shaped regions in J_z are present. In these regions magnetic reconnection operates, changing the topology of the magnetic field, an effect that it is not possible in the ideal regime, and reorienting its direction from the x - to the y -axis. These reconnection points divide the current sheets in topological islands that coalesce at later times. The evolution of the pressure follows a trend akin to the current density, with similar morphological features. In the region where the current dissipation is maximal, i.e. mostly inside magnetic islands, the maximum of the pressure is also reached due to the intense associated ohmic heating.

In Fig. 10 we present for all numerical schemes the time evo-

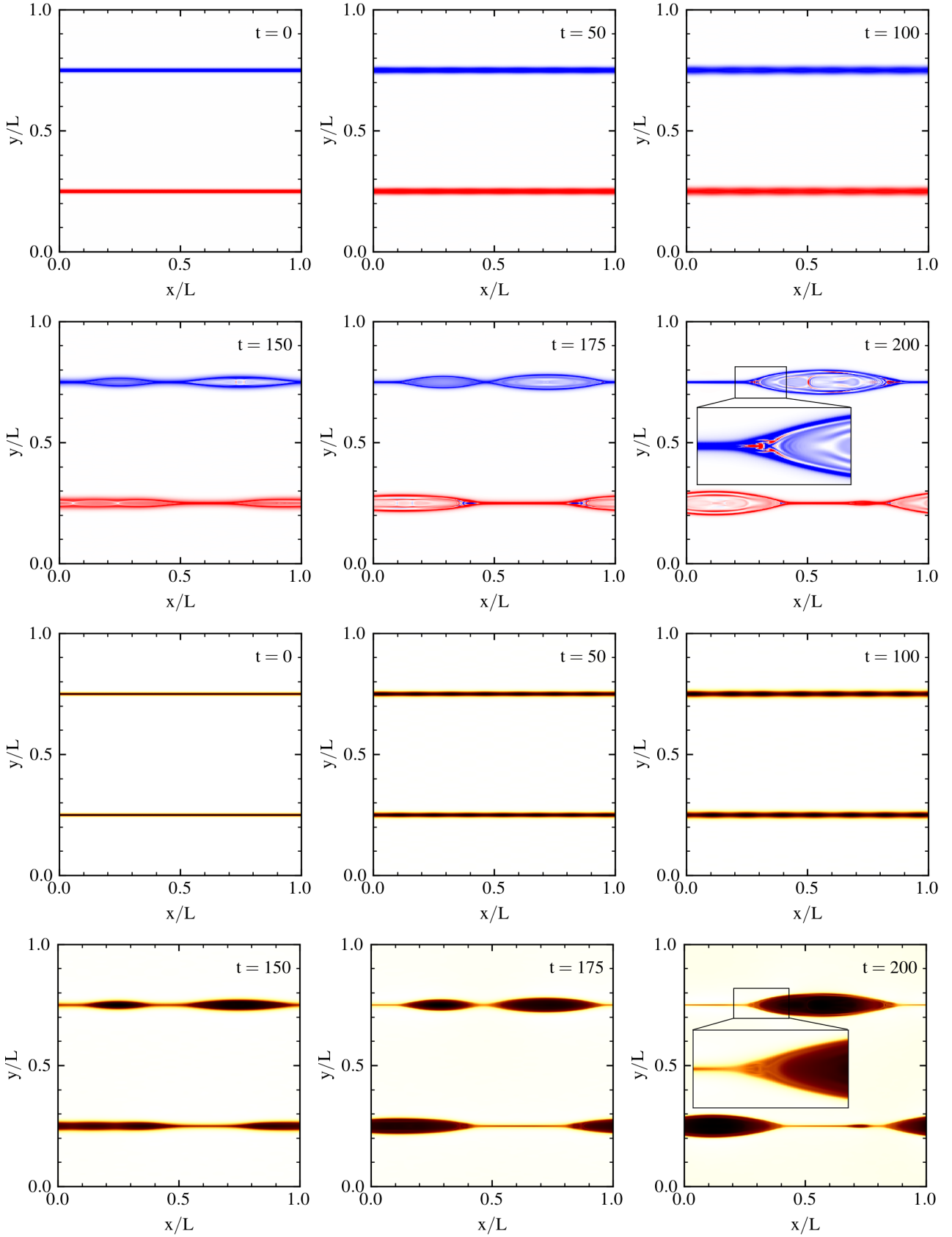


Figure 9. Time evolution of the out-of-plane current density J_z (top panels) and gas thermal pressure (bottom panels) of the magnetic reconnection simulation performed with the implicit CT scheme. Each snapshot has been taken at the time (normalized to t_A) indicated in each panel. Note the development of the X-point reconnection regions for times $t \gtrsim 100 \times t_A$ in the J_z snapshots, where the topology of the magnetic field is modified. The insets in the last panels show a magnified portion of the upper magnetic island.

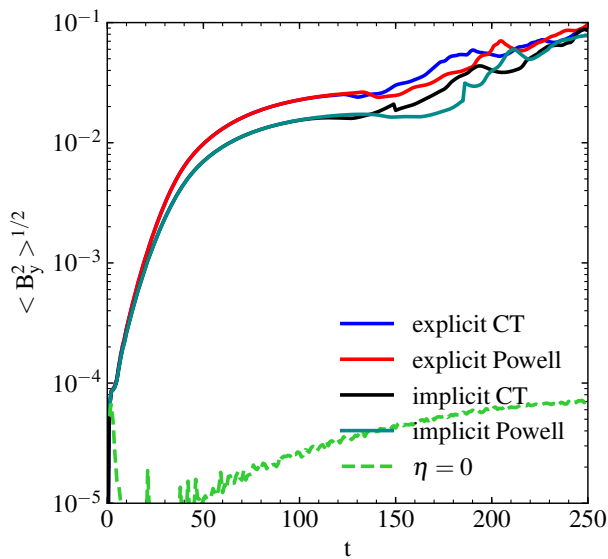


Figure 10. Volume-weighted average magnetic field along the y -direction as a function of time for the magnetic reconnection simulation (tearing instability) performed with different implementations of ohmic diffusivity as indicated in the legend. After an exponential increase at early times, the growth rate decreases sensibly after $t \sim 50 \times t_A$, although the field value keeps increasing steadily. Overall, the Powell and CT schemes agree quite well in their predictions. However, the implicit implementation predicts lower magnetic field values at times $t \gtrsim 25 \times t_A$. The discrepancy is about a factor of 2 at $t \approx 150 t_A$ to then reduce at the end of the examined time span. The green dashed line shows the evolution of the B_y rms amplitude for a non-resistive plasma. Note that in this case the growth rate of the field is much more reduced compared to the resistive simulation and the tearing instability does not develop although numerical reconnection is present to some extent.

lution of the volume-weighted rms values of the B_y component as a proxy for the evolution of the instability. The fraction of magnetic energy in the y -component of the field at the initial time is zero, so its evolution reflects the growth of the instability and the amount of reconnection occurring in the system. It is evident that in the linear regime of the instability (at very early times) the B_y rms value increases exponentially. At very early times ($t \sim t_A$) there is a wiggle in the B_y rms amplitude, which is likely due to our choice of perturbing the y -component of the gas velocity only rather than *both* gas velocity and magnetic field y -components based on an analytic solution of the tearing instability mode (e.g. Rembiasz et al. 2017). For $t \simeq 50 t_A$, the growth rate decreases sensibly, although the average B_y field keeps steadily increasing. In general, the Powell and the CT schemes give consistent results across all the examined time span. There is a difference in the final values of the B_y component between the explicit and implicit time integration, with the latter giving consistently lower values after a time of $t \gtrsim 25 t_A$ has elapsed. The difference reaches a maximum of about a factor of 2 at late times ($t \approx 150 t_A$) to then reduce at the end of the simulated time span. This trend is an indication that the implicit schemes are slightly more diffusive than their explicit counterparts. We ascribe this behaviour to the first-order and non-strictly conservative treatment of the Joule heating term in the implicit schemes (see equation 18). To investigate whether this could be the cause of the observed difference, we reran the magnetic reconnection test with the explicit schemes, but using the same first-order treatment for

the Joule heating term as in the implicit implementation. We find a closer agreement in the evolution of the rms B_y values in this case between explicit and implicit schemes, thus confirming that the additional diffusivity is caused by the treatment of the Joule term. The green dashed line shows the evolution of the B_y rms amplitude for a non-resistive plasma, in which η has been fixed to zero. Theoretically, the tearing instability, and the associated magnetic reconnection, can not develop in this configuration. However, any code introduces a finite amount of numerical resistivity due to the discretization of the equations governing the system. This numerical resistivity, which is dependent on resolution, can lead to magnetic reconnection that is entirely numerical in nature, and if it is large enough trigger the onset of the instability. It can be appreciated from the figure that there is an increase of the B_y rms amplitude due to this effect. However, the growth is much more reduced compared to the resistive simulation and the tearing instability does not develop at the resolution presented here. This is not the case for lower resolution realizations of this set-up, in which the amplitudes reached by the B_y field are comparable to the ones obtained with the onset of the tearing instability mode. In particular, degrading the resolution by a factor of 4 in both directions leads to the development of the instability for purely numerical reasons. Summarizing, these results illustrate the ability of our implementations to handle complex non-ideal MHD applications, which include ohmic resistivity.

5 MAGNETIZED CLOUD COLLAPSE

As another application of our scheme, we study next the gravitational collapse of a magnetized sphere and compare the outcome of simulations performed in the ideal and non-ideal MHD case. This system represents an important astrophysical problem as this set-up can be considered as an idealized model of the formation of a protostar.

The initial conditions for this problem are taken from Pakmor et al. (2011), which are an adaptation of those presented in Hennebelle & Fromang (2008). They consist of a spherical cloud of uniform density with a radius of $R_0 = 0.015$ pc. The cloud is embedded in a more tenuous atmosphere with a small transition region at the boundary. The initial mass of the cloud is $1 M_\odot$, which implies an initial density of 4.8×10^{-18} g cm $^{-3}$. With this initial density the free-fall time is 3×10^4 yr. The atmosphere surrounding the cloud is 100 times less dense than the cloud. At the beginning of the calculation the gas in the cloud rotates as a rigid body with a period of 4.7×10^5 yr. The simulation domain is a box of side length 0.06 pc and is filled with a uniform magnetic field with a strength of $30 \mu\text{G}$ directed in the same direction of the angular momentum of the gas. The gas follows a barotropic equation of state given by (see Hennebelle & Fromang 2008)

$$P = \rho c_0^2 \sqrt{1 + (\rho/\rho_c)^{4/3}}, \quad (50)$$

where $c_0 = 0.2$ km s $^{-1}$ and $\rho_c = 10^{-13}$ g cm $^{-3}$. Inflow/outflow boundary conditions are applied at all sides of the domain. We start the simulation with a Cartesian mesh with 128^3 cells, but we allow for the refinement of gas cells whose free-fall time-scale becomes smaller than 10 times its sound-crossing time-scale. With this criterion, we basically resolve the local Jeans length with at least 10 resolution elements. To avoid an excessive number of gas cells as the simulation progresses, we limit their volume to a minimum value of 5×10^{-17} pc 3 , which is equivalent to an effective resolution

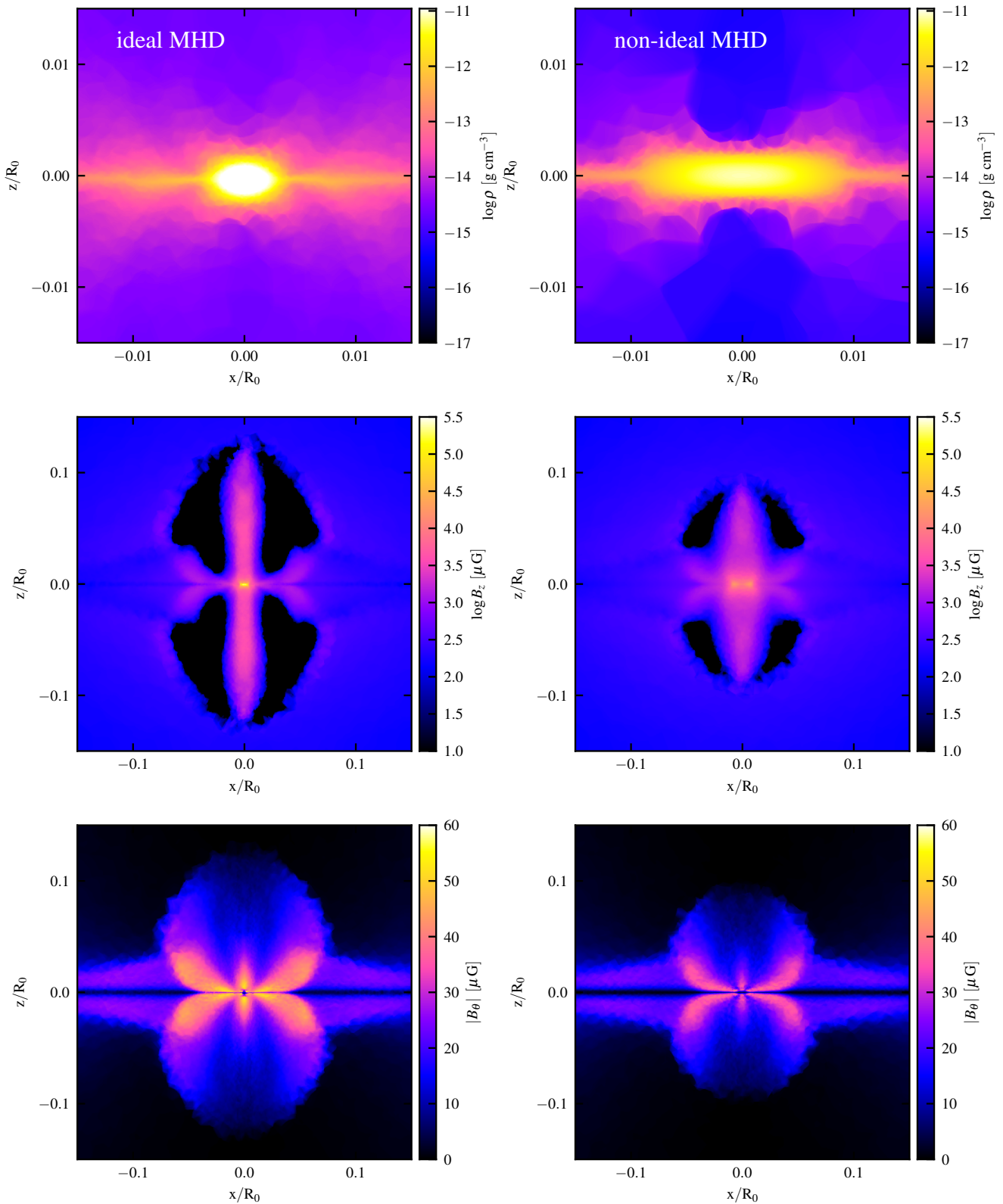


Figure 11. Collapse of a magnetized cloud in the ideal (left-hand column) and non-ideal (right-hand column) MHD case. The panels show a slice (of depth equal to 0.2 times the side length of the projection) through the centre of the simulated domain in the xz -plane. The top row shows a zoom-in of the volume-weighted gas density on the central region ($0.03 R_0$), where most of the mass of the cloud has collapsed, whereas the central and the bottom rows display the density-weighted magnetic field in the z - and azimuthal directions on a larger scale ($0.3 R_0$), respectively. The main effect of ohmic diffusivity in the calculation is to reduce the strength of magnetically-driven outflows (and of the global magnetic field strength) and to favour the formation of a larger disc-like structure in the central regions. All the panels are displayed at $t = 1.13 t_{\text{ff}}$.

of 16384^3 resolution elements (see [Hennebelle & Fromang 2008](#); [Pakmor et al. 2011](#)). In the simulation with ohmic resistivity, performed with the explicit Powell scheme, we use a spatially constant resistivity $\eta = 10^{18} \text{ cm}^2 \text{ s}^{-1}$. We note that this calculation is meant to be an idealized collapse model, and we therefore do not account for the variation of resistivity with gas properties (such as chemical composition and ionization state), a task that is non-trivial and outside the scope of this paper. However, the chosen resistivity value is appropriate for densities $n \gtrsim 10^{12} \text{ cm}^{-3} \simeq 1.67 \times 10^{-12} \text{ g cm}^{-3}$, assuming a fully hydrogen composition (see also [Machida et al. 2007](#), Fig. 1). These densities are reached in the regions surrounding the protostar in our set-up.

The choice of the explicit Powell scheme was also adopted on the basis that the ratio between the resistive and the CFL time-step (see equation 7) reaches a minimum value of about four at the end of the simulated time span ($1.13 t_{\text{ff}}$). So in terms of the size of the time-step, the advantages of using an implicit scheme are limited for this set-up. However, we would like to mention two important aspects: (i) the value of the resistivity might be larger than the one that we have adopted at higher densities ([Nakano et al. 2002](#); [Machida et al. 2007](#)), and (ii) we have imposed a minimum size to the gas cells in the simulation, effectively limiting the maximum resolution that can be achieved. Both factors contribute to keep the ratio of time-steps large enough that explicit schemes are a more convenient choice with respect to implicit schemes for this particular set-up. Increasing the resistivity value or the resolution of the simulation (or a combination of both) may render implicit schemes competitive with explicit schemes for this calculation.

Fig. 11 presents the output of the simulations in the ideal (left-hand column) and resistive (right-hand column) cases at the final time $t = 1.13 t_{\text{ff}}$. The rows show slices (of depth equal to 0.2 times the side length of the projection) through the centre of the simulated domain in the xz -plane (the z -axis coincides with the cloud's rotation axis) of the volume-weighted gas density (top) and the density-weighted magnetic field in the z - (middle) and azimuthal (bottom) directions. The density panels display the results on a smaller scale ($0.03 R_0$) compared to the magnetic field panels ($0.3 R_0$). In the ideal MHD case, results are similar to those found by [Pakmor et al. \(2011\)](#). At the centre of the domain a protostar is formed, which is surrounded by a disc of material. Compression of the gas due to the collapse has amplified the initial magnetic field to values of about $10^5 \mu\text{G}$ close to the protostar in the z -direction and to $\sim 70 \mu\text{G}$ in the azimuthal direction immediately above and below the mid-plane of the disc. The amplification of the magnetic field also causes the launching of magnetically driven outflows reaching distances in excess of $\sim 0.1 R_0$ from the protostar in the z -direction. The inclusion of ohmic resistivity changes this picture. In particular, the amplification of the field is less pronounced because of the diffusive effects. As a consequence, gas outflows are less strong (i.e. they reach a smaller distance from the protostar) and also the gas distribution in the protostar region is different, featuring a more thick and extended disc-like structure. These results are in line with numerical studies of star-forming clouds highlighting the importance of ohmic diffusion on the transport of angular momentum (e.g. [Dapp & Basu 2010](#)) and the generation of magnetically driven gas outflows (e.g. [Matsushita et al. 2017](#)), and further validate the applicability of our non-ideal MHD schemes to complex astrophysical systems. We caution again that the detailed effects of ohmic resistivity on the cloud collapse depend on the exact value of η as a function of the gas properties. This is a non-trivial task to accomplish and our simulations have not attempted

such detailed modelling resorting, instead, to a constant value for the resistivity.

6 SUMMARY AND CONCLUSIONS

Magnetic fields are an essential component of many physical processes that influence the evolution of the objects populating the Universe. Although in many astrophysical circumstances magnetic fields can be well modelled in the ideal MHD approximation, there are phenomena in which non-ideal effects such as ohmic resistivity, ambipolar diffusion and the Hall effect play an essential role. It is therefore desirable to extend the capabilities of numerical MHD codes to treat such non-ideal terms in order to faithfully model these phenomena.

In this paper, we have made a step in this direction by focusing on the inclusion of ohmic terms, which appear in the MHD equations when the gas resistivity is non-zero, in the moving-mesh code AREPO. The code has two main approaches for treating MHD, namely a [Powell et al. \(1999\)](#) divergence cleaning scheme and a CT method ([Mocz et al. 2014, 2016](#)) that evolves the vector potential to ensure the $\nabla \cdot \mathbf{B} = 0$ constraint. We have implemented the resistive terms for both techniques with explicit and implicit time integration. This allows for a high degree of flexibility in treating MHD problems in which diffusivity plays a role. In particular, the implicit time integration treatment makes it possible to circumvent the restrictive time-step CFL condition ($\propto \Delta x^{-2}$) necessary to guarantee the stability of explicit time integration schemes for diffusive phenomena. These explicit schemes are adopted in many non-ideal MHD simulation codes (see e.g. [Masson et al. 2012](#); [Mignone et al. 2012](#); [Hopkins 2017](#)), owing to their relatively simple implementation. However, the quadratic spatial resolution scaling of their CFL condition renders them impractical for high-resolution applications.

We have tested our implementation in problems of increasing physical complexity. We have first confirmed that the magnetic field properly diffuses, in the absence of any gas dynamics, in all our implementations. To this end we have performed a classical 1D diffusion test of a Gaussian magnetic field configuration recovering the expected evolution. We have also extended this test to a 2D configuration and found that all our implementations yielded the expected results. In particular, we demonstrated that, regardless of the scheme employed, second-order convergence is achieved.

We have then proceeded to include gas dynamics in our test problems by studying the decay of Alfvén waves due to a finite resistivity of the plasma. We have tested all our schemes in two different initial configurations: a progressive wave and a superposition of two waves travelling in opposite directions that give rise to a stationary wave configuration. In both cases, all the schemes that we have implemented recovered the expected exponential decay of the magnetic field strength, and showed second-order convergence also in the presence of gas dynamics. We note that ohmic resistivity not only causes the magnetic field to diffuse – and, in particular, to decay exponentially in this problem – but also increases the plasma temperature through Joule dissipation. In the diffusion of an Alfvén wave (both in the progressive and stationary configurations), Joule dissipation increases uniformly the gas pressure as the intensity of the magnetic field declines. This behaviour is captured correctly by our schemes, although the treatment of Joule heating is different (second versus first-order accurate) between explicit and implicit schemes, and this difference may sometimes have a more pronounced impact on the results (see Fig. 10).

As a first application, we have investigated magnetic reconnection in a plasma configuration that develops the tearing instability (Furth et al. 1963). The study of the emergence of this instability is complicated by the fact that any numerical scheme introduces non-physical numerical resistivity due to the discretization procedure. This numerical resistivity can affect the results, especially in the low-resistivity regime, which is interesting for the modelling of real systems such as the solar corona. It is therefore important that the level of numerical resistivity is lower than the physical resistivity that is considered in the calculations, which can be achieved by adopting a high enough resolution in the simulation. We took care of this aspect by first running a version of this problem with zero resistivity for increasingly high resolution until no instability due to numerical effects was present in the calculation. We then introduced physical resistivity in the system and studied its evolution. All our schemes were able to capture the onset and the evolution of the instability into to the non-linear regime. Furthermore, our simulations clearly showed the emergence of X shaped regions in the out-of-plane current density J_z , demonstrating that intense magnetic reconnection is occurring. These regions of strong magnetic reconnection divide the plasma into magnetic islands that eventually coalesce.

Finally, to further test our implementation on a problem directly relevant for astrophysical applications and in particular for star formation studies, we have examined the gravitational collapse of a magnetized rotating cloud (Hennebelle & Fromang 2008). We have demonstrated that for high-enough, but admissible, values of the ohmic resistivity there are visible effects on the density gas distribution around the emerging protostar, the amplification of the magnetic field due to the collapse, and the strength of the magnetically driven outflows. In particular, compared to the ideal MHD case (see also Pakmor et al. 2011), the gas in the vicinity of the protostar is distributed in a more thick and extended disc-like structure, the final magnetic field strength is lower and the resulting gas outflows are weaker and less extended, in broad agreement with previous non-ideal MHD work (e.g. Dapp & Basu 2010; Matsushita et al. 2017).

To conclude, we have presented a first implementation of non-ideal MHD terms in the moving-mesh code AREPO. Interesting applications of the new code capabilities include the study of massive star formation in atomic cooling haloes (Becerra et al. 2015), or the role of magnetic fields on small-scale star formation (Hull et al. 2017) and its correlations to supersonic turbulence in star-forming cores (Mocz et al. 2017). We intend to pursue these lines of research in future work.

ACKNOWLEDGEMENTS

We thank the referee for their detailed comments on the manuscript. MV acknowledges support through an MIT RSC award, the support of the Alfred P. Sloan Foundation, and support by NASA ATP grant NNX17AG29G. RK and PM acknowledge support from NASA through Einstein Postdoctoral Fellowship grant numbers PF7-180163 (RK) and PF7-180164 (PM) awarded by the *Chandra* X-ray Center, which is operated by the Smithsonian Astrophysical Observatory for NASA under contract NAS8-03060. VS acknowledges support through sub-project EXAMAG of the Priority Programme 1648 SPPEXA of the German Science Foundation. VS and RP are also supported by the European Research Council through ERC-StG grant EXAGAL-308037. The simulations were performed on the joint MIT-Harvard computing cluster supported

by MKI and FAS. All the figures in this work were created with the MATPLOTLIB graphics environment (Hunter 2007).

REFERENCES

- Bai X.-N., 2015, *ApJ*, **798**, 84
 Basu S., Ciolek G. E., 2004, *ApJ*, **607**, L39
 Basu S., Dapp W. B., 2010, *ApJ*, **716**, 427
 Becerra F., Greif T. H., Springel V., Hernquist L. E., 2015, *MNRAS*, **446**, 2380
 Beck R., Wielebinski R., 2013, *Magnetic Fields in Galaxies*. p. 641, doi:10.1007/978-94-007-5612-0_13
 Béthune W., Lesur G., Ferreira J., 2017, *A&A*, **600**, A75
 Cheng X., Guo Y., Ding M., 2017, *Science in China Earth Sciences*, **60**, 1383
 Cox D. P., 2005, *ARA&A*, **43**, 337
 Crank J., Nicolson P., Hartree D. R., 1947, *Proceedings of the Cambridge Philosophical Society*, **43**, 50
 Dapp W. B., Basu S., 2010, *A&A*, **521**, L56
 Dolag K., Stasyszyn F., 2009, *MNRAS*, **398**, 1678
 Dolag K., Bartelmann M., Lesch H., 1999, *A&A*, **348**, 351
 Dolag K., Bartelmann M., Lesch H., 2002, *A&A*, **387**, 383
 Dolag K., Komatsu E., Sunyaev R., 2016, *MNRAS*, **463**, 1797
 Falle S. A. E. G., 2003, *MNRAS*, **344**, 1210
 Ferretti L., Giovannini G., Govoni F., Murgia M., 2012, *A&ARv*, **20**, 54
 Fermi E., 1949, *Physical Review*, **75**, 1169
 Ferrière K. M., 2001, *Reviews of Modern Physics*, **73**, 1031
 Fromang S., Hennebelle P., Teyssier R., 2006, *A&A*, **457**, 371
 Furth H. P., Killeen J., Rosenbluth M. N., 1963, *Physics of Fluids*, **6**, 459
 Gressel O., Turner N. J., Nelson R. P., McNally C. P., 2015, *ApJ*, **801**, 84
 Harris E. G., 1962, *Nuovo Cim.*, **23**, 115
 Hennebelle P., Fromang S., 2008, *A&A*, **477**, 9
 Hennebelle P., Teyssier R., 2008, *A&A*, **477**, 25
 Hennebelle P., Commerçon B., Joos M., Klessen R. S., Krumholz M., Tan J. C., Teyssier R., 2011, *A&A*, **528**, A72
 Henson V. E., Yang U. M., 2002, *Applied Numerical Mathematics*, **41**, 155
 Hopkins P. F., 2017, *MNRAS*, **466**, 3387
 Hopkins P. F., Raives M. J., 2016, *MNRAS*, **455**, 51
 Hull C. L. H., et al., 2017, *ApJ*, **842**, L9
 Hunter J. D., 2007, *Computing In Science & Engineering*, **9**, 90
 Iffrig O., Hennebelle P., 2017, *A&A*, **604**, A70
 Kannan R., Springel V., Pakmor R., Marinacci F., Vogelsberger M., 2016, *MNRAS*, **458**, 410
 Kannan R., Vogelsberger M., Pfrommer C., Weinberger R., Springel V., Hernquist L., Puchwein E., Pakmor R., 2017, *ApJ*, **837**, L18
 Klimchuk J. A., 2006, *Sol. Phys.*, **234**, 41
 Kotera K., Olinto A. V., 2011, *ARA&A*, **49**, 119
 Krasnopolsky R., Li Z.-Y., Shang H., 2010, *ApJ*, **716**, 1541
 Landi S., Bettarini L., 2012, *Space Sci. Rev.*, **172**, 253
 Landi S., Londrillo P., Velli M., Bettarini L., 2008, *Physics of Plasmas*, **15**, 012302
 Lesur G., Kunz M. W., Fromang S., 2014, *A&A*, **566**, A56
 Li P. S., McKee C. F., Klein R. I., Fisher R. T., 2008, *ApJ*, **684**, 380
 Li Z.-Y., Krasnopolsky R., Shang H., 2011, *ApJ*, **738**, 180
 Mac Low M.-M., Norman M. L., Konigl A., Wardle M., 1995, *ApJ*, **442**, 726
 Machida M. N., Inutsuka S.-i., Matsumoto T., 2007, *ApJ*, **670**, 1198
 Marinacci F., Vogelsberger M., 2016, *MNRAS*, **456**, L69
 Marinacci F., Vogelsberger M., Mocz P., Pakmor R., 2015, *MNRAS*, **453**, 3999
 Marinacci F., et al., 2017, preprint, (arXiv:1707.03396)
 Masson J., Teyssier R., Mulet-Marquis C., Hennebelle P., Chabrier G., 2012, *ApJS*, **201**, 24
 Matsushita Y., Machida M. N., Sakurai Y., Hosokawa T., 2017, *MNRAS*, **470**, 1026
 Mestel L., Spitzer Jr. L., 1956, *MNRAS*, **116**, 503

- Mignone A., Bodo G., Massaglia S., Matsakos T., Tesileanu O., Zanni C., Ferrari A., 2007, *ApJS*, **170**, 228
- Mignone A., Zanni C., Tzeferacos P., van Straalen B., Colella P., Bodo G., 2012, *ApJS*, **198**, 7
- Mocz P., Vogelsberger M., Hernquist L., 2014, *MNRAS*, **442**, 43
- Mocz P., Pakmor R., Springel V., Vogelsberger M., Marinacci F., Hernquist L., 2016, *MNRAS*, **463**, 477
- Mocz P., Burkhardt B., Hernquist L., McKee C. F., Springel V., 2017, *ApJ*, **838**, 40
- Mouschovias T. C., 1976a, *ApJ*, **206**, 753
- Mouschovias T. C., 1976b, *ApJ*, **207**, 141
- Nakano T., Nishi R., Umebayashi T., 2002, *ApJ*, **573**, 199
- Ntormousi E., Hennebelle P., André P., Masson J., 2016, *A&A*, **589**, A24
- Pakmor R., Springel V., 2013, *MNRAS*, **432**, 176
- Pakmor R., Bauer A., Springel V., 2011, *MNRAS*, **418**, 1392
- Pakmor R., Marinacci F., Springel V., 2014, *ApJ*, **783**, L20
- Pakmor R., Springel V., Bauer A., Mocz P., Muñoz D. J., Ohlmann S. T., Schaal K., Zhu C., 2016, *MNRAS*, **455**, 1134
- Pakmor R., et al., 2017, *MNRAS*, **469**, 3185
- Parker E. N., 1983, *ApJ*, **264**, 642
- Powell K. G., Roe P. L., Linde T. J., Gombosi T. I., De Zeeuw D. L., 1999, *Journal of Computational Physics*, **154**, 284
- Rembiasz T., Obergaulinger M., Cerdá-Durán P., Aloy M.-Á., Müller E., 2017, *ApJS*, **230**, 18
- Saad Y., Schultz M. H., 1986, *SIAM Journal on Scientific and Statistical Computing*, **7**, 856
- Santos-Lima R., de Gouveia Dal Pino E. M., Lazarian A., 2012, *ApJ*, **747**, 21
- Seaton D. B., Bartz A. E., Darnel J. M., 2017, *ApJ*, **835**, 139
- Seifried D., Pudritz R. E., Banerjee R., Duffin D., Klessen R. S., 2012, *MNRAS*, **422**, 347
- Shu F. H., Adams F. C., Lizano S., 1987, *ARA&A*, **25**, 23
- Springel V., 2010, *MNRAS*, **401**, 791
- Stone J. M., Gardiner T. A., Teuben P., Hawley J. F., Simon J. B., 2008, *ApJS*, **178**, 137
- Tilley D. A., Balsara D. S., 2011, *MNRAS*, **415**, 3681
- Vallée J. P., 1998, *Fundamentals Cosmic Phys.*, **19**, 319
- Zhu C., Liu R., Alexander D., McAtteer R. T. J., 2016, *ApJ*, **821**, L29
- de Avillez M. A., Breitschwerdt D., 2005, *A&A*, **436**, 585